Turbulence and Radiation in Stratocumulus Topped Marine Boundary Layer: A Case Study from VOCALS-REx

Virendra P. Ghate[1], Bruce A. Albrecht[2], Mark A. Miller[1], Alan Brewer[3], and Christopher W. Fairall[3]

1. Department of Environmental Sciences, Rutgers University

2. Division of Meteorology and Physical Oceanography, University of Miami

3. Physical Science Division, NOAA-ESRL

Corresponding Author
Virendra P. Ghate
14 College farm road,
New Brunswick, NJ 08901
Ph: 848-932-6744
Fax: 732-932-8644
Email: vghate@envsci.rutgers.edu

ABSTRACT

Observations made during a 24 hour period as part of the VAMOS Ocean-Cloud-Atmosphere-Land Study Regional Experiment (VOCALS-REx) are analyzed to study the radiation and turbulence associated with stratocumulus topped marine boundary layer (BL). The first fourteen hours exhibited a well-mixed BL with an average cloud top radiative flux divergence of ~130 W m^{-2}; the BL was decoupled during the last 10 hours with negligible radiative flux divergence. The averaged radiative cooling very close to the cloud top was -9.04 K $hour^{-1}$ in coupled conditions and -3.85 K $hour^{-1}$ in decoupled conditions. Data from the vertically pointing Doppler cloud radar and Doppler lidar were combined to yield the vertical velocity structure of entire BL. The averaged vertical velocity variance and updraft mass-flux during coupled conditions were higher than those during decoupled conditions at all levels by factor of 2 or more. The vertical velocity skewness was negative in the entire BL during coupled conditions, while it was weakly positive in the lower third of the BL and negative above during decoupled conditions. A formulation of velocity scale is proposed which includes the effect of cloud top radiative cooling in addition to the surface buoyancy flux. When scaled by the velocity scale, the in-cloud values of vertical velocity variance, updraft mass-flux and coherent downdrafts had similar magnitude during the coupled and decoupled conditions. The coherent updrafts which exhibited a constant profile in the entire BL during both the coupled and decoupled conditions scaled well with the convective velocity scale to a value of 0.6.

1. INTRODUCTION

Marine stratocumulus clouds have significantly higher albedo than the underlying ocean surface and when present they reflect greater amount of incoming solar radiation back to the space. Due to their low cloud top heights, the longwave radiation emitted by these clouds is comparable to that emitted at the ocean surface whereupon they produce a minimal impact on the longwave radiation energy budget. The net radiative effect of these clouds is to cool the ocean surface. Vast layers of stratocumulus clouds are observed over the Eastern subtropical oceans with the largest subtropical stratocumulus layer present over the South-East Pacific region west of the coast of Chile and Bolivia (Klein and Hartmann, 1993). These extensive stratocumulus layers impose overcast upon a large area of the ocean surface and thereby impart a significant influence on the Earth's radiation budget. So it is essential to represent these clouds and the associated processes accurately in Global Climate Models (GCM) simulations aimed at predicting the future climate. But these clouds occur at spatial scales that are poorly resolved by GCMs and hence their cloudiness and associated effects need to be parameterized, and many parameterizations have been proposed for this purpose including Klein and Hartmann (1993), Bretherton et al. (2004) etc. While cumulus parameterizations in GCMs perform admirably in some circumstances and in some regions, they misrepresent marine stratocumulus in many others and remain a major source of uncertainty in the climate forecasts (Bony and Dufresene, 2006).

Marine stratocumulus clouds are inexorably linked to turbulence in the marine boundary layer (BL) and many observational (Frisch et al 1995; Ghate et al. 2010 etc) and modeling studies (Mechem et al. 2012; Zhu et al. 2005; Stevens et al. 1999; Moeng et al. 1996) have focused on this link. Turbulent kinetic energy generation in the stratocumulus topped marine BL is maintained through radiative cooling near cloud top which mainly occurs in the longwave

(LW) radiation spectral band (Lilly, 1968). This LW radiative cooling is offset during the daytime by radiative heating resulting from the absorption of shortwave (SW) radiation, primarily by water vapor, and with insufficient turbulent kinetic energy generation to mix the full depth of the marine boundary layer, it becomes stratified into two isolated layers – this is known as decoupling. This decoupling of the cloud layer from its sub-cloud layer prevents moisture resupply to the cloud layer potentially leading to its thinning or dissipation during the daytime. This decoupling phenomenon is not captured well in GCMs due to inadequate representation of the cloud-radiation-turbulence interactions (Medeiros et al. 2012).

Decoupled BLs were routinely observed during the VAMOS Ocean-Cloud-Atmosphere-Land Study Regional Experiment (VOCALS-REx) (Wood et al. 2011; Jones et al. 2011; Bretherton et al. 2010) and we use these data to study the differences in the BL turbulence structure during coupled and decoupled episodes. Data collected onboard R/V Ronald H. Brown on November 27, 2008 are the foundation of the present study. Satellite imagery captured by the Moderate Resolution Infrared Spectroradiometer (MODIS) onboard the Aqua satellite during the study period is shown in Fig 1 along with the Eastward track of the R/V Ronald H. Brown. Instrumentation onboard R/V Ronald Brown in described in detail by Wood et al (2011), and hence in the next section we have only described the subset of the instrumentation onboard R/V Brown used in this study. Beyond this interlude to describe the instrumentation and processing methods, data are classified according by mixing state as determined by thermodynamic structure and the links between mixing state and cloud arrangement are reconnoitered.

2. INSTRUMENTATION AND RADIATION TRANSFER MODEL

The instrumentation suite present onboard R/V Brown included a motion-stabilized, vertically-pointing Doppler cloud radar, a motion-stabilized scanning Doppler lidar, a laser ceilometer, a microwave radiometer and turbulent/radiative flux suite. Balloon borne radiosondes were also launched every 4 hours. A 95-GHz cloud radar was operated exclusively in vertically-pointing mode (Moran et al. 2012) and recorded the Doppler spectrum and its first three moments; Reflectivity, mean Doppler velocity and Doppler spectrum width. The radar was operating at a 3 Hz and 20 m temporal and spatial resolution respectively. A High Resolution Doppler Lidar (HRDL) operating at 2 μm wavelength (Grund et al. 2001; Tucker et al. 2009) was pointing vertically for 10 minutes and scanning either in a Range Height Indicator (RHI) or Plan Position Indicator (PPI) mode for the other 10 minutes in alternate cycles and recorded the aerosol backscatter signal strength and Doppler velocity at 2 Hz and 30 m resolution. The HRDL data from the vertically pointing mode only are used in this study. A 905 nm wavelength laser ceilometer was used to measure the first three optical cloud base heights at 15 sec and 15 m resolution. Broadband radiometers recorded the downwelling shortwave radiation (0.3 to 3 micron) and downwelling longwave radiation (4 to 50 micron) each minute. Accompanying these instruments was a flux suite accumulating high temporal resolution temperature, wind and humidity measurements used to calculate the surface sensible heat flux (SHF) and latent heat flux (LHF) according to the technique described by Fairall et al (2003). A microwave radiometer (MWR) recorded the sky brightness temperatures at 23.8 GHz and 31.4 GHz from which the atmospheric column integrated water vapor (IWV) and liquid water path (LWP) were estimated every 30 seconds (Zuidema et al. 2005).

Radiative heating rate profiles were computed every second using the Rapid Radiative Transfer Model (RRTM) using radiosonde moisture and temperature measurements and measurement-constrained cloud microphysical properties as in Mather et al. (2007). These simulations possessed a resolution of 20 m from surface till 1.5 km, 500 m from 2 km till 12 km and 1 km from 12 km till 60 km. Greenhouse gas concentrations were supplied to RRTM based upon the latest measurements, most notably a carbon dioxide concentration of 388.5 ppm. Due to inadequate information about the aerosol properties, radiative effects due to aerosols were neglected in the RRTM simulations, however the remote ocean location and overcast nature of the study area likely justifies their exclusion in our study (Tomlinson et al. 2007).

Accounting for cirrus clouds in the RRTM simulations was problematic because the maximum observation range of the radar and HRDL were 4 km and 6 km respectively, but none of the soundings launched during the day showed an increased relative humidity at high levels that would have been indicative of cirrus and they were neglected in the RRTM simulations. Also, the satellite imagery (Fig 1) during the day did not show any cirrus clouds. Since we are invoking the independent pixel approximation by using a one-dimensional radiative transfer model, we neglect any three dimensional radiative effects. Notwithstanding, the study conditions observed are of a single layer stratocumulus cloud or of clear sky periods, so we anticipate the 3-D effects to be minimal.

3. CASE DESCRIPTION

The radar observed reflectivity and mean Doppler velocity for 27 November 2008 are shown in Figure 2 along with the Lifting Condensation Level (LCL) calculated using surface meteorological measurements per the formulation by Bolton (1980) and the ceilometer observed

lowest cloud base height. Variability is evident throughout the day in these observations as indicated by systematic excursions in the cloud top height over periods of several hours. A thin stratus layer was detected by the ceilometer from 1800 to 2400 UTC, but was undetected by the cloud radar due to its lower sensitivity (higher cloud detection threshold signal-to-noise ratio). Intermittent nimbostratus produced intrusions of evaporating precipitation into the sub-cloud layer as revealed by negative Doppler velocities below the ceilometer cloud base that were detected from 0400 till 0900 UTC and from 1300 till 1600 UTC. Excellent correspondence between the ceilometer detected cloud base height and the LCL was noted from 0000 UTC till 1400 UTC after which the two levels became discordant. Such a thermodynamic structure is symptomatic of a BL that was well mixed and coupled to the surface (Jones et al., 2011) from 0000 till 1400 UTC and decoupled thereafter. A rapid increase in the LCL towards the last 10 minutes of the 24^{th} hour is noteworthy, but the BL was decoupled for the majority of that hour and these final 10 minutes are inconsequential to the statistics presented in this study. The linchpin of this study is that for the first time the updraft and downdrafts from cloud top to the near surface in this important cloud system were successfully measured from a moving ship when Doppler velocity from the 95 GHz and HRDL were combined, even during precipitation events.

The HRDL backscatter and Doppler velocity and the ceilometer observed first cloud base height are shown in Figure 3. Attenuation by cloud droplet scattering prevents the HRDL from penetrating significantly above the optical cloud base thereby limiting its sampling to the sub-cloud layer only. Since only the data from the vertically pointing mode are shown, data gaps correspond to the periods when the HRDL was performing RHI or PPI scans. As the cloud layer thinned after 1800 UTC, and especially during the clear sky conditions observed during 2200

UTC, the HRDL was able to observe the entire BL. Backscatter decreased after 1800 UTC suggesting lower aerosol concentration during this period, perhaps due to scavenging by precipitation, though a definitive cause for this decrease cannot be determined from these observations.

Profiles of potential temperature and mixing ratio from six radiosondes launched four hours apart (Fig 4) depict a nearly constant inversion base height during the day that corresponded well with the average cloud top heights observed by the cloud radar in the vicinity of radiosonde launch times. Except for the radiosonde launched on 0800 UTC, all the soundings showed relatively constant potential temperature and mixing ratio profiles, especially in the sub-cloud layer, though the 2000 UTC sounding indicated decoupling with a weak inversion around 850 m. This inversion coincided with the LCL during that hour (850 m), confirming that the cloud layer was thermodynamically decoupled from the sub-cloud layer. A weak inversion can also be seen in the sounding launched at 1600 UTC at around 900 m.

The case-mean profile of the longwave radiative flux, shortwave radiative flux and net radiative flux as simulated by RRTM is shown in Fig 4 along with the associated heating rate profiles. A positive value of flux denotes a net downward flux while a negative value denotes a net upward flux. The longwave flux was almost constant in the sub-cloud layer and in the free troposphere, but showed a slight increase near cloud base and a sharp decrease near cloud top. This decrease of the longwave flux above cloud top is indicative of cloud droplet and moisture gradient emitted longwave radiation present near the boundary layer inversion. Absorption of shortwave radiation by water vapor caused the shortwave flux to increase slightly from the surface toward cloud base and from cloud base till the cloud top with a constant profile in the free troposphere. Predictably, the longwave radiative flux was negative in the entire troposphere,

the shortwave radiative flux positive, and the net radiative flux also positive. Net radiative fluxes were about 150 W m^{-2} in the sub-cloud layer and about 100 W m^{-2} in the free troposphere and the net radiative flux showed a slight increase in the cloud layer and a sharp decrease near the BL inversion.

Radiative flux profiles produced a longwave heating rates that were weakly positive near cloud base and strongly negative (~3.5 k $hour^{-1}$) near cloud top. The zigzag structure of the LW heating rate in the middle of the cloud layer is an artifact of averaging samples with different cloud thickness rather than changes in radiation. Shortwave heating rate increased from the cloud base till the cloud top with a sharp decrease above that. Consequently, net radiative heating loosely echoed the profile of longwave radiative heating with a diminished magnitude. All of the radiative heating rates were almost zero in the sub-cloud layer and above the BL inversion. These radiative fluxes and heating rate profiles are in general agreement with previous modeling (Moeng et al., 1996; Stevens et al., 1999) and observational studies (Duda et al., 1991) in marine stratocumulus clouds.

Downwelling LW radiation at the surface during the study period (Fig. 5) was constant throughout the day with a decrease observed between 2100 and 2300 UTC as the cloud layer thinned and eventually disappeared. Downwelling SW radiation loosely followed the solar insolation exhibiting variability typically associated with passing clouds, although changes in the cloud microphysical properties might also have contributed to this variability. The surface LHF (Fig. 5) exceeded 60 W m^{-2} except when it decreased sporadically between 0500 and 0900 UTC. A plausible explanation for these decreases is an increase in the surface specific humidity due to drizzle evaporation during those times (see Fig. 3). The SHF was always negligibly low: 6 W m^{-2}, with a peak around 1300 UTC and nearly constant around 2 W m^{-2} from 0000-0800 and 1800-

2400 UTC. Predominance of the LHF in this region is in agreement with the previous long-term observations (Ghate et al. 2009; de Szoeke et al. 2012).

Column integrated water vapor (IWV) as recorded by a microwave radiometer remained fairly constant around 1.3 cm throughout the entire day while the liquid water path (LWP) varied with peaks corresponding to changes in the cloud depth. A peak value of LWP of 400 gm^{-2} corresponded with the heaviest drizzle event with other relative peaks also associated with the precipitation events. Coincidence between LWP and drizzle intensity is circumstantially supportive of the hypothesized dependence of precipitation susceptibility on the LWP (Caldwell and Bretherton, 2009). Although no cloud layer was present from 2200 UTC to 2300 UTC, the radiometer recorded a LWP of 50 g m^{-2} corresponding to a bias in the retrieval of LWP from the MWR.

The surface buoyancy flux (B) was calculated using the SHF and LHF and is shown in Fig 6. It closely follows the SHF with a minimum of ~2 W m^{-2}, maximum of ~13 W m^{-2} and average value of 7.65 W m^{-2}. Hence, the buoyancy production at the surface varied little during the entire day. In addition to B generating convection at the surface through heating of air parcels, radiative cooling predominantly in the upper half of the BL also generates convection through buoyancy reversal. The shortwave, longwave and net radiative divergence from LCL height till boundary layer height (ΔF_{rad}) is shown in Fig 6. The choice of height for calculating the radiative divergence is made so as to be consistent with the calculation of a radiative velocity scale discussed later. Since the radiative flux profiles (Fig 4) vary a little in the lower half of the boundary layer and in the free troposphere, the calculated divergence is very similar to that calculated over the entire boundary layer depth or the lower troposphere. During nighttime, the longwave radiative divergence is relatively constant at around -120 W m^{-2}. While during the

daytime, due to absorption of solar radiation by water vapor, the net divergence increased to a value above zero (heating) around 1500 UTC (0900 local time). The net radiative divergence was above zero till 2100 UTC (1500 local time), with a drop around 2000 UTC due to disappearance of the cloud layer. Although the cloud layer was intermittently present after 2000 UTC, the LW divergence was about -50 W m^{-2} mainly because of the jump in mixing ratio across the BL inversion.

The surface convective velocity scale (w^*_{sfc}) was also calculated using the following equation per Stull (1988) and the LCL height (Z_{LCL}) as the scaling height along with the acceleration due to gravity (g) and the mean surface virtual potential temperature ($\overline{\theta_v}$)

$$w^*_{sfc} = \left(\frac{g \times Z_{LCL}}{\overline{\theta_v}} \times \left(\overline{w'\theta'_v} \right)_{sfc} \right)^{1/3}$$

The w^*_{sfc} varied little during the period (Fig 6) with a mean value of ~0.6 m s^{-1}. Although the LCL height changed from a value of ~1050 m during the earlier part of the day to ~850 m during the later part together with some changes in the surface buoyancy flux, due to the one-third power dependence there was little change in w^*_{sfc}. We have chosen the LCL height as the length scale in the calculation of w^*_{sfc}, since the thermals originating from the surface will encounter the first thermodynamically different layer at the LCL.

Lock and MacVean (1999) proposed a complementary radiative velocity scale (w^*_{rad}), which used the change in the radiative flux over the entire boundary layer and the boundary layer depth as a scaling height. Their formulation was based on the original results by Bohnert (1993) who proposed the w^*_{rad} formulation for clear-air boundary turbulence. We have modified the Lock and MacVean (1999) formulation to the following equation which uses the distance between the LCL height and BL inversion base height (Z_{thick}), air density (ρ), specific heat at

constant pressure (c_p) and mean potential temperature of the layer ($\overline{\theta}$). The air density was assumed to be constant at 1.2 kg m^{-3}.

$$w^*_{rad} = \left(\frac{g \times Z_{thick}}{\rho \times c_p \times \overline{\theta}} \times \left(-\Delta F_{rad} \right) \right)^{1/3}$$

Instead of using the entire boundary layer depth as a scaling height, we have used the distance between the boundary layer inversion base height and the LCL height as a scaling height. Hence we essentially assume that the downdrafts generated due to radiative cooling near inversion base will encounter the first thermodynamically different layer at the LCL. Based on aircraft measurements Tjernstrom and Rogers (1996) proposed a similar formulation using the buoyancy flux at the cloud top and cloud thickness as a scaling height. Z_{thick} (not shown) varied from ~450 m in the earlier part of the day to over 600 m during the later part of the day. w^*_{rad} was ~1.2 m s^{-1} during the nighttime and decreased to zero around 1500 UTC. Except for a few wiggles, it remained zero till 2200 UTC (1600 Local Time). Although no cloud layer was present during 2300 UTC, due to a low amount of heating in the SW spectrum but significant cooling in the LW spectrum, w^*_{rad} was around 0.8 m s^{-1}.

The surface convective velocity scale and the radiative velocity scale were combined to yield the total velocity scale (velocity scale from here on) which is the cubic averaged of the two. This velocity scale (w*) was over 1.2 m s^{-1} during the nighttime and decreased to a value of ~0.6 m s^{-1} during the daytime. Since the radiative cooling and surface heating of air is taken into account in the formulation of the velocity scale, it presents an opportunity to have a scaling variable for dynamical parameters under variety of conditions. However we acknowledge that drizzle evaporative cooling can also be a factor in controlling the BL dynamics (Ackerman et al. 2009) and the current formulation of w* does not take it into account.

4. DATA PROCESSING AND CASE-MEAN STATISTICS

Data from the Doppler cloud radar and HRDL were averaged to produce a 1 Hz, 30 m uniform grid for further processing. The backscatter signal from the HRDL operating at 2 μm wavelength is sensitive to aerosols that have negligible fall velocity and therefore act as tracers of the vertical wind, so the HRDL Doppler velocity tracked the air vertical motion. Cloud radar operating at 95 GHz is sensitive to cloud and precipitation size droplets and the cloud droplets have negligible fall velocity, so the Doppler velocity during cloud only conditions (<-20 dBZ) represents air motions (Frisch et al. 1995; Ghate et al. 2010). Precipitation fall velocity must be subtracted from the observed Doppler velocity to determine the air vertical motion and, among the several published techniques that may be applied (Kollias et al. 2011), we chose a technique similar to Feingold et al. (1999) and Frisch et al. (1995). A cubical fit between reflectivity and mean Doppler velocity was computed for 5 min averaging windows and this fit was assumed to represent the contribution from precipitation. The fall velocity yielded by the empirical fit was then subtracted from the 1 Hz observed Doppler velocity to yield the vertical air motion.

Vertical velocity profiles from near the surface to the top of the cloud layer for every second were constructed by combining the HDRL and cloud radar measurements using the ceilometer cloud base height as the terminus of the HDRL profile and the beginning of the cloud radar profile. Further, due to the possibility of low frequency (more than 30 mins) drift in vertical motion correction and pointing angle stabilization, the hourly mean vertical velocity was subtracted from the retrieved velocities at each level. These hourly mean values were less than 0.1 m s^{-1} at all levels during the day. While it is beyond the scope of this study to test the accuracy of the retrieval technique or to compare it with other techniques in the literature, the profiles of the vertical velocity and related parameters showed convincing consistency below and

above the cloud base. The average cloud base height was 1052 m and LCL was 990 m during the study period.

The level of BL turbulence is reflected in the average vertical velocity variance and its skewness, which are shown in Fig 7. Vertical velocity variance increased from 0.25 $m^2 s^{-2}$ to 0.45 $m^2 s^{-2}$ from 200 m until its peak at 1100 m and decreased towards cloud top, which is indicative of Turbulent Kinetic Energy (TKE) peaking at approximately 1100-1200 m. Negative vertical velocity skewness denoted that downdrafts were stronger than the updrafts in the entire BL with the difference between the two being greatest at 900 m. Structurally, this configuration indicates that the most turbulent region in the cloud consists of coexisting updrafts and downdrafts with a slight predisposition to contain some strong downdrafts whilst the region nearer to cloud base exhibits a considerably stronger predisposition to contain strong downdrafts, though it is less turbulent overall. Such a structure near cloud base could be driven by evaporating drizzle enhancing negative buoyancy just beneath cloud base that accelerates downdrafts just inside the cloud.

Conditionally sampled updraft and downdraft fractions (Fig. 7) reveal that in the lower half of the BL there are more updrafts than downdrafts while in the upper half of the BL there are about equal number of updrafts and downdrafts. The percentage of updrafts exceeding 0.25 m s^{-1} decreased from ~30% at 200 m to 25% at 900 m, but increased to 30% above 900 m. Comparatively, the percentage of downdrafts stronger than -0.25 ms^{-1} methodically decreased from ~30% at cloud top to ~25% at 200 m. In the BL as a whole, more downdrafts exceeded -1 ms^{-1} than updrafts exceeded 1 ms^{-1} and the percentage of these updrafts remained constant from 200 m till 600 m at ~4% and decreased to a minimum of 2% at 900 m. The percentage of updrafts stronger than 1 m s^{-1} and the vertical velocity variance coincidently peaked at 1100 m

(~6%) suggesting modulation of this variance by updrafts. Downdrafts stronger than -1 m s^{-1} increased in frequency from cloud top to a maximum of 9% at 900 m and then decreased almost linearly till 200 m. Coincident occurrence of a minima in the vertical velocity skewness and maxima in the downdrafts exceeding -1 m s^{-1} at 900 m suggests primary modulation of the negative vertical velocity skewness by the strongest downdrafts.

Updrafts and downdrafts that spanned the entire depth of the BL were defined as coherent and composite profiles of these features are shown in Fig 8. While the coherent updrafts experienced no acceleration and were almost constant at ~0.5 m s^{-1} from 200 m till 1000 m with a small peak at 1000 m and decrease above, the coherent downdrafts experienced a more complicated acceleration and deceleration structure. Downdrafts accelerated as they sank from the cloud top till 900 m where they peaked at -1.25 m s^{-1} and steadily decelerated to about 0.75 m s^{-1} at 200 m. Only ~4% of the updrafts and downdrafts were coherent, however, so the prevailing structure was discordant turbulence through the BL.

Convective parameterizations employ the updraft/downdraft mass-flux as a primary diagnostic variable and the specific mass flux (M) may be computed from these data using the classic plume decomposition technique proposed by Arakawa and Schubert (1974), which is given by

$$M = \sum_i \sigma_i \times \left(w_i - \overline{w}\right)$$

Where w is the vertical velocity, σ is the updraft fraction and $\overline{w}$ is the hourly mean vertical velocity. Mass flux was calculated for each velocity bin spaced at 0.1 m s^{-1} from -3 m s^{-1} to 3 m s^{-1} and these individual contributions to the total mass flux from each velocity bin are summed to produce the total mass flux at each height during each hour (the updraft component is summed from 0 to 3 m s^{-1}). These hourly values were averaged to produce a composite profile of the

updraft mass flux (Fig. 8), which loosely follows the profile of coherent updrafts. It remained constant from 200 m till 1000 m at ~0.2 m s^{-1} and exhibited a sharp increase leading to a maximum of approximately 0.25 m s^{-1} at 1100 m followed by a steady decline above.

To illustrate which velocity bins contribute the most to the total mass flux, the velocity binned mass-flux at four levels is shown in Fig. 9 along with the updraft mass-flux at each level. The updraft mass-flux peak value exceeds that of the downdraft mass-flux at each level and eddies with velocity of ~0.5 m s^{-1} are the predominant facilitators of the mass transport in the updraft regime at all levels. Downdraft eddies with velocity of -0.5 m s^{-1} are responsible for most of the mass-transport at 1200 m, while at 300 m the same is true for eddies with vertical velocity of -0.25 m s^{-1}. Predictably, the tail of the distribution of the downdraft mass-flux is longer than that of the updraft mass-flux at all levels given the negative vertical velocity skewness in the entire BL. Particularly, strong updraft eddies (>2 m s^{-1}) do not transport significant mass, while in contrast significant mass was transported by particularly strong downdraft eddies (<-2 m s^{-1}), especially at 900 m. The updraft and downdraft mass flux contributions are not entirely symmetrical about zero vertical velocity and the most substantial asymmetry is the confinement of the updraft mass flux contributions to a more narrow range of velocities, which is indicated by the steep roll-off toward larger velocities when compared to the downdraft contributions. Apart from this velocity range asymmetry, the updraft mass-flux is relatively constant at all the four levels (~0.2 m s^{-1}) except for a slight decrease at 900 m.

4. COUPLED VS DECOUPLED COMPARISON

Hourly statistics were further classified as coupled and decoupled based on the separation between LCL height and cloud base height. This conditional sampling produced a clear

bifurcation in the data in that the first fourteen hours were classified as coupled while the rest were classified as decoupled. The mean cloud base height during coupled hours was 995 m, while the same during decoupled hours was 1148 m, and the LCL height during coupled hours was 1052 m, while the same during decoupled hours was 904 m. Average cloud top heights for these two stability classifications were nearly constant (1330 and 1370 m), but there was a significant difference in the cloud thicknesses, which were 337 m during the coupled period and 265 m during the decoupled period.

Driving this thermodynamic stratification was the radiation fluxes and the associated heating rates (Fig 10). Consistent with past studies (Turton and Nicholls, 1987; Bretherton and Wyant, 1996), thermodynamic coupling was observed predominantly during the nighttime and in the early daylight hours when the shortwave radiation flux and associated heating rate were negligible. The net longwave flux during coupled conditions was around -30 Wm^{-2} in the sub-cloud layer, near-zero in the cloud layer and about -130 W m^{-2} above the inversion base, whereupon the longwave heating rates near cloud base were about 0.5 k $hour^{-1}$ and about -3.5 k $hour^{-1}$ near cloud top. As anticipated, net values of the radiation fluxes and heating rates echo those of longwave radiation.

Solar insolation substantially alters the radiation fluxes and the heating rates producing thermodynamic decoupling. The longwave fluxes were -50 W m^{-2} in the sub-cloud and cloud layer and about -150 W m^{-2} above the BL inversion during decoupled conditions. Shortwave fluxes increased almost linearly from surface value of 425 W m^{-2} to about 450 Wm^{-2} near cloud base in response to water vapor absorption and exhibited a sudden increase to 525 W m^{-2} in the cloud layer and above the BL inversion. Net radiative fluxes during the thermodynamically decoupled conditions were positive with a average value of ~360 W m^{-2} in the sub-cloud layer

and above the BL inversion. The net radiation flux peaked near cloud top at ~400 W m^{-2} with the increase being rather gradual followed by a sudden decrease above the cloud top. Longwave radiative heating near cloud base was negligible during decoupled conditions, unlike the coupled conditions, while radiative cooling near cloud top remained nearly the same as that during coupled conditions (~-3.5 k $hour^{-1}$). Shortwave radiative heating rates increased from near zero just below cloud base to about 1.8 K $hour^{-1}$ near cloud top followed by a sharp decrease above to near zero. The net radiative heating increased from cloud base to a peak of 1 k $hour^{-1}$ in the middle of the cloud and then decreased sharply to a value of -2 k $hour^{-1}$ near cloud top. Compared to the coupled conditions, the decoupled conditions had higher amount of cloud base heating and a lower amount of cloud top cooling.

Vertical velocity variance and skewness during coupled hours and decoupled hours were averaged and the composites are presented in Fig 11. Vertical velocity variances at all levels were higher when the BL was coupled and increased from 200 m till 500 m and then remained constant till 1000 m. Above 1000 m, the coupled vertical velocity variances varied rather widely, though a signature feature is the peak at around 1150 m. In contrast, the vertical velocity variance is appreciably lower and nearly constant at ~0.15 m^2 s^{-2} in the entire boundary layer during the decoupled conditions. During coupled conditions, the vertical velocity skewness was negative in the entire BL and decreased from 200 m to its lowest value at 900 m almost linearly, while above 900 m it increased to 0.1 at 1150 m and remained fairly constant above that. The vertical velocity skewness associated with thermodynamic decoupling decreased almost linearly from 200 m till 800 m and then remained constant above that. Positive vertical velocity skewness from 200 m till 500 m during decoupled periods is indicative of prevailing updrafts and suggests that the TKE is being generated by surface buoyancy, shear and other processes near the ocean

surface. The variance and skewness profiles for the coupled-decoupled distinction are similar to those reported by Hogan et al. (2009).

The conditionally sampled averaged updraft and downdraft fractions for coupled and decoupled conditions (Fig 12) reveal differing patterns of organization at different levels in the BL, most notably in the sub-cloud layer because it is most affected by radiatively-induced decoupling, evaporating drizzle, and shear-generated TKE at the ocean surface. Significant height-dependent variations in the sub-cloud layer are obvious in the thermodynamically coupled BL, but less obvious in the decoupled BL where apart from some subtle differences the height-dependent organization of updrafts and downdrafts is the same.

Focusing first on thermodynamically coupled conditions, the percent of the strongest updrafts (>1 ms^{-1}) remained fairly constant from 200 m till 900 m (~5%), exhibited a rapid increase in the clouds till 1150 m (~8%), and then decreased above that. The percentage of downdrafts stronger than -1 ms^{-1} increased from the cloud top to its maximum of ~15% at 1150 m and decreased below it almost linearly during coupled conditions. Contemplating thermodynamically decoupled conditions during which negligible amount of updrafts stronger than 1 ms^{-1} (<1%) are observed, the percent of downdrafts stronger than -1 ms^{-1} remained fairly constant from 200 m till 1000 m (~2%) and then peaked to a value of 10% at 1100 m with a decrease above that.

These data suggest the BL turbulent eddies updrafts during decoupled conditions are organized in a manner that produces fewer that can transport water vapor from the surface to the cloud layer, and that this reduction in the number of updrafts is increasingly extreme for the increasingly strong updrafts whereupon strong updrafts become nearly non-existent. Despite the

observation of negative skewness in these profiles, there are a higher percentage of updrafts than downdrafts because the downdrafts are narrow and intense and updrafts are broad and weak.

Averaged profiles of structurally coherent updrafts and downdrafts that span the depth of the BL (Fig. 13) show stark differentiation in which thermodynamically decoupled conditions possess notable symmetry between the updraft and downdraft profiles that are relatively devoid of accelerations, while coupled conditions exhibit large asymmetry and appreciable accelerations and decelerations. Constant vertical velocity profiles found in the decoupled condition probably reflect a small percentage of cases in which (1) circulations in the sub-cloud layer and cloud layer are phase-locked or (2) the thermodynamic decoupling has been breached by a convective circulation fueled by the small amount of Convective Available Potential Energy (CAPE) that exists when the BL is decoupled.

During thermodynamically coupled conditions the coherent downdrafts accelerated as they move downward in the cloud layer and reach a maximum velocity in the vicinity of cloud base and steadily decelerate as they sink toward the surface. Conversely, coherent updrafts during the coupled conditions move air steadily from the surface through the lower portion of the cloud where it then experiences a rapid acceleration through a relatively shallow layer just above 1000 m before decelerating toward cloud top. The ratio of the coherent updrafts to the coherent downdrafts (not shown) in the middle of the BL was less than unity during coupled conditions, while it was closer to unity during decoupled conditions.

The updraft mass-fluxes observed in thermodynamically coupled and decoupled conditions are vastly different, with the mass flux in coupled conditions being double of that in decoupled conditions in a majority of the BL. As in the case of the coherent drafts, the decoupled condition provides less structural variation in the mass flux as a function of height. Two distinct

regions of relatively larger mass flux separated by a local minimum are noted in the coupled case: one maximum in the sub-cloud layer from 200 m till 700 m at ~0.25 m s^{-1} and another in the cloud layer peaking at around 1100 m. The position of the local minimum near the center of the BL is probably due to its relative location due to the energy sources that are driving the mass flux, which are located near cloud top and at the surface.

Mass-fluxes binned by vertical velocity during coupled and decoupled conditions quantify the relative contributions of individual vertical velocity bins to the total mass flux (Fig. 14), which as previously noted was almost half of that during coupled conditions at all levels. Consistent with this reduced mass flux in decoupled conditions was a reduction in the vertical velocity of the eddy responsible for the maximum transport compared to the coupled conditions in both updraft and downdraft regimes, yet there was little decrease in the actual mass-transport caused by these eddies, especially in the downdraft regime. Updrafts stronger than 1.5 m s^{-1} are responsible for mass-transports during the coupled conditions while almost negligible transport is being done by updrafts stronger than 1 m s^{-1} during decoupled conditions. Significant mass transports are done by eddies stronger than -1.5 m s^{-1} in the downdraft regime during coupled conditions, while eddies stronger than -1.5 m s^{-1} cause no transport during the decoupled conditions. The kurtosis of the distribution in the downdraft regime is much higher during decoupled conditions than during the coupled conditions primarily due to the gradual decrease in the mass-flux with an increasing downdraft velocity observed during coupled conditions. At 900 m during coupled conditions the kurtosis was 1.76 and during decoupled conditions it was 5.81.

In past studies focusing on BL clouds attempts have been made to use the convective velocity scale as a scaling parameter (e.g. Tjernström and Rogers, 1996; Tjernström and Rune, 2003; Neggers et al. 2007 etc.) so as to be ultimately used in prognostic parameterizations. The

averaged profile of vertical velocity variance, updraft mass-flux, coherent updrafts and coherent downdrafts scaled by the convective velocity scale w* for the coupled and decoupled conditions are shown in Fig 15. The in-cloud vertical velocity variance collapses to a value of ~0.4 when scaled by the square of convective velocity scale, the result seems consistent with past studies which modeled the in-cloud variance as a function of BL depth, w* and CAPE (e.g. Grant and Brown, 1999). The in-cloud updraft mass-flux also collapsed to a value of ~0.2 when scaled by the w*. The sub-cloud layer vertical velocity variance and updraft mass-flux however did not scale consistently with the w* for the distinction. The coherent updrafts scaled to a value of ~0.6 in the entire BL when scaled by the w*. The coherent downdrafts scaled to a value of ~-0.8 when scaled by the convective velocity scale for the thermodynamic distinction.

5. SUMMARY AND DISCUSSION

This study describes an analysis of data collected from multiple instruments as part of VOCALS-REx during a 24 hour period onboard the R/V Ronald H. Brown. This analysis is unique, to the best knowledge of the authors, in that coincident data from a vertically-pointing Doppler cloud radar and Doppler lidar, both motion-stabilized, are combined to observe the turbulence structure of a stratocumulus topped marine BL. These data are complemented by measurements of the LWP and IWV from a microwave radiometer and surface flux measurements.

The IWV, surface SHF and surface LHF did not vary significantly during the 24-hour study period, suggesting that changes in BL structure by caused by advection of different air mass or changes in sea surface temperature were minimal. Radiative transfer model calculations made at a high resolution showed a LW radiative cooling at the top of the BL during the entire

period which was entirely offset by the SW heating during the later part of the day. The surface buoyancy flux and the radiative flux divergence between the LCL and inversion base was also combined to formulate a convective velocity scale. Fourteen hours exhibited coupled BL conditions, with the LCL and cloud base height differing by ~50 m, while the remainder of the 24-hour period exhibited decoupled BL with the LCL and cloud base height differing by more than 200 m.

Mean values of the all the variables along with the values averaged over the hours classified as coupled and decoupled are tabulated in Table 1. Cloud thickness was higher during the coupled BL conditions and the net radiative cooling near BL inversion base during decoupled conditions was ~42% of that observed during coupled conditions. As hypothesized by previous studies, this net difference in radiative cooling is responsible (along with drizzle evaporative cooling) for decoupling of the stratocumulus topped BL. Our data demonstrates important structural differences in the turbulence profiles depending on thermodynamic structure: the average vertical velocity variance during decoupled conditions was only one third of its value during coupled conditions.

Negative vertical velocity skewness was observed in both coupled and decoupled conditions in the cloud layer, but in the sub-cloud layer smaller magnitudes of positive skewness were observed during decoupled conditions due to the decreased strength of downdrafts. Conditionally sampling the data to identify coherent vertical velocity structures that spanned the entire depth of the BL revealed the same relative relationship in negative skewness as present in the data set as a whole. Philosophically, the notion of a “coherent” turbulence profile in decoupled conditions is rather counterintuitive since the basic definition of decoupling is based upon perceived incoherence in the turbulence profile. It is possible to reconcile this paradox if

(1) circulations in the sub-cloud layer and cloud layer are phase-locked or (2) the thermodynamic decoupling has been breached by a convective circulation fueled by the small amount of Convective Available Potential Energy (CAPE) that exists when the BL is decoupled. In either case, it is likely that the exchanges between the upper and lower portions of the BL when it is decoupled still occur during a small percentage of events (<5%).

Of paramount importance in this study is the characterization of the mass flux because its diagnosis is critical in the convective transports in models of all varieties and it was determined that the updraft mass-flux during coupled conditions was twice that during the decoupled conditions. Maximum transport of mass is accomplished in coupled conditions by eddies with vertical velocities between ± 0.75 ms^{-1} and ± 0.50 ms^{-1} and in decoupled conditions by eddies with vertical velocities <0.50 ms^{-1}. Contemplating these results in the context of cloud formation suggests that these updraft velocities may limit the aerosol nucleation process in some circumstances, especially when the BL is decoupled. This latter possibility could potentially limit the implementation of the Twomey effect during the daytime and, hence, mitigate or negate its impacts in this cloud system.

A proposed convective velocity scale which takes into account the radiative cooling near BL top in addition to the surface buoyant production was used as a scaling parameter for the dynamical properties. The in-cloud vertical velocity variance, in-cloud updraft mass-flux and in-cloud coherent downdrafts when scaled by the velocity scale had a similar value during the coupled and decoupled conditions. The coherent updrafts which had a constant profile in the entire BL also scaled well with the velocity scale. This suggests that the proposed velocity scale could be used to calculate the strength of the coherent updrafts within the BL along with the in-cloud vertical velocity variance and in-cloud updraft mass-flux. Since, the formulation of the

velocity scale does not take into account the cooling induced by drizzle evaporation; consistent scaling of the coherent updrafts with w* suggests that the coherent updrafts are little affected by drizzle evaporative cooling.

Our results highlight the differences in the turbulence structure of a stratocumulus topped marine BL during coupled and decoupled conditions. While we have characterized the turbulence and radiation structure, we expect decoupling to be a result of combination of reduction in the cloud top radiative cooling and due to drizzle evaporative cooling, but the dominant process responsible for the decoupling and the cloud-radiation-turbulence coupling during this transition can be only further explored through a LES type model coupled to a bin-microphysics scheme. Therein, we expect the results presented in this study to be helpful for future modeling and observational studies.

Acknowledgments: The authors wish to thank the officers and crew of the NOAA ship Ronald H. Brown for great support during the cruise. This work is supported by NOAA's Climate Project Office (ESS program).

REFERENCES

Ackerman, A. S., M. C. Vanzanten, B. Stevens, V. Savic-Jovcic, C. S. Bretherton, A. Chlond, J-C Golaz, H. Jiang, M. Khairoutdinov, S. K. Krueger, D. C. Lewellen, A. Lock, C-H Moeng, K. Nakamura, M. D. Petters, J. R. Snider, S. Weinbrecht and M. Zulauf 2009: Large-eddy simulations of a drizzling, stratocumulus-topped marine boundary layer. *Mon. Weath. Rev.*, **137**, 1083-1110.

Arakawa, A. and W. H. Schubert, 1974: Interaction of a Cumulus cloud ensemble with the large-scale environment, Part I. *J. Atmos. Sci.*, **31**, 674–701.

Bohnert, M., 1993: A numerical investigation of cloud-topped planetary boundary layers. Ph.D. Thesis, Dept. of Mech. Engr., Stanford University.

Bolton, D, 1980: The computation of equivalent potential temperature. *Mon. Wea. Rev.*, **108**, 1046–1053.

Bony, S. and J.-L. Dufresne, 2005: Marine boundary layer clouds at the heart of tropical cloud feedback uncertainties in climate models, *Geophys. Res. Lett.*, **32**, L20806, doi:10.1029/2005GL023851.

Bretherton, C. S. and M. C. Wyant, 1997: Moisture transport, lower-tropospheric stability, and decoupling of cloud-topped boundary layers. *J. Atmos. Sci*., **54**, 148–167.

Bretherton, C. S., J. R. McCaa, H. Grenier, 2004: A new parameterization for shallow cumulus convection and its application to marine subtropical cloud-topped boundary layers. Part I: Description and 1D results. *Mon. Wea. Rev.*, **132**, 864–882.

Bretherton, C. S., R. Wood., R. C. George, D. Leon, G. Allen, and X. Zheng, 2010: Southeast Pacific stratocumulus clouds, precipitation and boundary layer structure sampled along

20° S during VOCALS-REx, *Atmos. Chem. Phys.*, **10**, 10639-10654, doi:10.5194/acp-10-10639-2010,

Caldwell, P. and C. S. Bretherton, 2009: Large eddy simulation of the diurnal cycle in Southeast Pacific stratocumulus. *J. Atmos. Sci.*, **66**, 432–449.

Deardorff, J. W., 1980: Cloud-top entrainment instability. *J. Atmos. Sci.*, **37**, 131-147.

de Szoeke, S. P., S. Yuter, D. Mechem, C. W. Fairallm C. Burleyson and P. Zuidema, 2012: Observations of stratocumulus clouds and their effect on the eastern Pacific surface heat budget along 20°S., *J. Climate, accepted*.

Duda, D. P., G. L. Stephens and S. K. Cox, 1991: Microphysical and radiative properties of marine stratocumulus from tethered balloon measurements. *J. Appl. Meteor.*, **30**, 170–186.

Fairall, C. W., E. F. Bradley, J. E. Hare, A. A. Grachev and J. B. Edson, 2003: Bulk parameterization of air–sea fluxes: updates and verification for the COARE algorithm. *J. Climate*, **16**, 571–591.

Feingold, G., A. Frisch, B. Stevens, and W. Cotton, 1999: On the relationship among cloud turbulence, droplet formation and drizzle as viewed by Doppler radar, microwave radiometer and lidar. *J. Geophys. Res*., **104(D18),** 22195-22203.

Frisch, A. S., D. H. Lenschow, C. W. Fairall, W. H. Schubert and J. S. Gibson, 1995: Doppler radar measurements of turbulence in marine stratiform cloud during ASTEX. *J. Atmos. Sci.*, **52**, 2800–2808.

Ghate, V. P., B. A. Albrecht, C. W. Fairall and R. A. Weller, 2009: Climatology of surface meteorology, surface fluxes, cloud fraction, and radiative forcing over the southeast Pacific from buoy observations. *J. Climate*, **22**, 5527–5540

Ghate, V. P., B. A. Albrecht, and P. Kollias, 2010: Vertical velocity structure of non-precipitating continental boundary layer stratocumulus clouds, *J. Geophys. Res.*, **115**, D13204, doi:10.1029/2009JD013091.

Grund, C. J., and Coauthors, 2001: High-resolution Doppler lidar for boundary layer and cloud research. *J. Atmos. Oceanic Technol.*, **18**, 376–393

Grant A. L. M. and Brown A. R., 1999: A similarity hypothesis for shallow-cumulus transports. *Quart. J. Roy. Meteorol. Soc.*, **125**, 1913–1936.

Hogan, R., J., A. L. M. Grant, A. J. Illingworth, G. N. Pearson and E. J. O'Connor. 2009: Vertical velocity variance and skewness in clear and cloud-topped boundary layers as revealed by Doppler lidar. *Q. J. R. Meteorol. Soc.* **135**: 635–643

Jones, C. R., C. S. Bretherton, and D. Leon, 2011: Coupled vs. decoupled boundary layers in VOCALS-REx, *Atmos. Chem. Phys*., **11**, 7143-7153, doi:10.5194/acp-11-7143-2011.

Klein, S. A. and D. L. Hartmann, 1993: The seasonal cycle of low stratiform clouds. *J. Climate*, **6**, 1587–1606.

Kollias, P., J. Rémillard, E. Luke, and W. Szyrmer, 2011: Cloud radar Doppler spectra in drizzling stratiform clouds: 1. Forward modeling and remote sensing applications, *J. Geophys. Res.*, **116**, D13201, doi:10.1029/2010JD015237.

Lock, A. P., and M. K. MacVean, 1999: A parameterization of entrainment driven by surface heating and cloud-top cooling. *Quart. J. Roy. Meteor. Soc.*, **125**, 271-300.

Lilly, D. K., 1968: Models of cloud topped mixed layers under a strong inversion. *Quart. J. Roy. Meteor. Soc.*, **94,** 292–309.

Mather, J. H., S. A. McFarlane, M. A. Miller, and K. L. Johnson 2007: Cloud properties and associated radiative heating rates in the tropical western Pacific, *J. Geophys. Res.*, **112**, D05201, doi:10.1029/2006JD007555.

Mechem, D. B., S. E. Yuter, S. P. de Szoeke, 2012: Thermodynamic and Aerosol Controls in Southeast Pacific Stratocumulus. *J. Atmos. Sci.*, **69**, 1250–1266.

Medeiros, B., D. Williamson, C. Hannay, and J. Olson, 2012: Southeast Pacific stratocumulus in the Community Atmosphere Model. *J. Climate*. doi:10.1175/JCLI-D-11-00503.1, in press.

Moeng, C-H, J. C. Wyngaard, 1984: Statistics of conservative scalars in the convective boundary layer. *J. Atmos. Sci.*, **41**, 3161–3169.

Moeng, C.-H., Cotton, W. R., Bretherton, C., Chlond, A., Kairoutdinov, M., Krueger, S., Lewellen, W. S., MacVean, M. K., Pasquier, J. R. M., Rand H. A., Siebesma, A. P., Stevens, B., and Sykes, R. I., 1996, Simulation of a stratocumulus-topped planetary boundary layer: Intercomparison among different numerical codes, *Bull. Amer. Meteorol. Soc*., **77**, 261–278.

Moran, K., S. Pezoa, C. W. Fairall, C. Williams, T. Ayers, A. Brewer, S. P. deSzoeke and V. Ghate, 2011: A motion-stabilized w-band radar for shipboard observations of marine boundary-layer clouds. *Bound. Layer Meteor.*, 143, 3-24. doi: 10.1007/s10546-011-9674-5

Neggers, R. A. J., B. Stevens and J. D. Neelin, 2007: Variance scaling in shallow-cumulus-topped mixed layer. *Quart. J. Roy. Meteor. Soc.*, **133**, 1629-1641.

Stevens B., Moeng, C.-H., Ackerman, A. S., Bretherton, C. S., Chlond, A., de Roode, S.,Edward, J., Golaz, J.- C., Diang, H., Khairontdinor, M., Kirkpatrick, M. P., Lewellen, D. C., Lock,

A., Muller, F., Stevens, D. E., Whelan, E., and Zhu, P., 2005, Evaluation of large-eddy simulation via observations of nocturnal marine stratocumulus, *Misc. Wea. Rev.*, **133**, 1443–1462.

Stevens B., C-H. Moeng, and P. P. Sullivan, 1999: Large-eddy simulations of radiatively driven convection: sensitivities to the representation of small scales, *J. Atmos. Sci*. **56**, 3963–3984.

Stull, R. B., 1988: *An introduction to boundary layer meteorology*. Kluwer Academics, 666 pp

Tjernström, M., and D. P. Rogers, 1996: Turbulence structure in decoupled marine stratocumulus: A case study from the ASTEX field experiment. *J. Atmos. Sci.*, **53**, 598–619.

Tjernström, M., and A. Rune, 2003: The structure of gradually transforming marine stratocumulus during the ASTEX first Lagrangian experiment. *Quart, J. of Roy. Meteor. Soc.*, **129**, 1071-1100

Tomlinson, J. M., R. Li, and D. R. Collins, 2007: Physical and chemical properties of the aerosol within the southeastern Pacific marine boundary layer. *J. Geophys. Res.*, **112**, D12211, doi:10.1029/2006JD007771.

Tucker S.C., W. A. Brewer, R. M. Banta, C. J. Senff, S. P. Sandberg, et al., 2009: Doppler lidar estimation of mixing height using turbulence, shear, and aerosol profiles. *J. Atmos. Ocean. Tech.*, **26**, 673-688

Turton, J. D. and S. Nicholls, 1987: Diurnal variation of stratocumulus. *Quart. J. Roy. Meteor. Soc.*, **113**, 969-1009.

Wood, R., C. R. Mechoso, C. S. Bretherton, R. A. Weller, B. Huebert, F. Straneo, B. A. Albrecht, H. Coe, G. Allen, G. Vaughan, P. Daum, C. W. Fairall, D. Chand, L.

Gallardo Klenner, R. Garreaud, C. Grados, D. S. Covert, T. S. Bates, R. Krejci, L. M. Russell, S. de Szoeke, A. Brewer, S. E. Yuter, S. R. Springston, A. Chaigneau, R. Toniazzo, P. Minnis, R. Palikonda, S. J. Abel, W. O. J. Brown, S. Williams, J. Fochesatto, J. Brioude and K. N. Bower: The VAMOS Ocean-Cloud-Atmosphere-Land Study Regional Experiment (VOCALS-REx): goals, platforms, and field operations, *Atmos. Chem. Phys.*, **11**, 627-654, doi:10.5194/acp-11-627-2011, 2011

Zhu, P., and Coauthors, 2005: Intercomparison and interpretation of single-column model simulations of a nocturnal stratocumulus-topped marine boundary layer. *Mon. Wea. Rev.*, **133**, 2741-2758

Zuidema, P., E. Westwater, C. Fairall and D. Hazen, 2005: Ship-based liquid water path estimates in marine Stratocumulus. *J. Geophys. Res.*, **110**, D20206, doi:10.1029/2005JD005833

Table 1: Mean values of variables during the entire case, coupled boundary layer conditions and decoupled boundary layer conditions. Averaged values for the entire boundary layer of the parameters pertaining to the vertical velocity are reported. Please refer to the text regarding the acronyms.

Variable	**Case Mean**	**Coupled Boundary Layer**	**Decoupled Boundary Layer**
Int. Water Vapor (cm)	1.32	1.32	1.31
Liquid Water Path(g m^{-2})	164	197	119
Sensible Heat Flux (W m^{-2})	2.14	2.25	2
Latent Heat Flux (W m^{-2})	75.82	74.54	77.61
Downwelling Longwave Radiation (W m^{-2})	377.20	385.27	365.95
Downwelling Shortwave Radiation (W m^{-2})	196.39	29.46	429.25
Lifting Condensation Level (m)	990	1052	904
Cloud Base Height (m)	1052	995	1149
Cloud Top Height (m)	1344	1322	1374
Cloud Thickness (m)	316	337	265

Net Heating Rate at Inversion Base (K hour^{-1})	-6.88	-9.04	-3.85
w^*_{sfc} (m s^{-1})	0.59	0.60	0.57
w^*_{rad} (m s^{-1})	0.74	1.07	0.26
w^* (m s^{-1})	0.94	1.14	0.66
Vertical Velocity Variance (m^2 s^{-2})	0.31	0.43	0.13
Vertical Velocity Skewness	-0.28	-0.36	-0.15
Coherent updrafts (m s^{-1})	0.59	0.71	0.41
Coherent Downdrafts (m s^{-1})	-0.79	-0.97	-0.50
Amount of updrafts stronger than 1 m s^{-1} (%)	2.69	4.22	0.32
Amount of downdrafts stronger than -1 m s^{-1} (%)	4.32	6.37	1.14
Updraft mass-flux (m s^{-1})	0.16	0.20	0.10

1

FIGURE CAPTIONS

Figure 1: Visible image as captured by the MODIS Aqua satellite on 27 November 2008 at 1855 UTC (1255 local time). The red line shows the eastward track of the Ronald H. Brown for that day.

Figure 2: Reflectivity (top) and mean Doppler velocity (bottom) as recorded by the vertically pointing 95 GHz Doppler Cloud radar on 27 November 2008. The ceilometer recorded cloud base height is shown in black while the lifting condensation level calculated using surface measurements is shown in red.

Figure 3: The signal to noise ratio (top) and Doppler velocity (bottom) as recorded by the HRDL when it was pointing vertically upwards on 27 November 2008. The ceilometer recorded cloud base height is shown in black.

Figure 4: Profiles of potential temperature and mixing ratio (top panels) as reported by the radiosondes launched during that day and profiles of averaged longwave (LW), shortwave (SW) and net radiative flux along with the associated heating rates (bottom panels).

Figure 5: Downwelling shortwave radiation and downwelling longwave radiation (top), surface sensible heat flux and surface latent heat flux (middle) and integrated water vapor and liquid water path (bottom) for 27 November 2008. The local time is six hours behind UTC.

Figure 6: Surface buoyancy flux (top), shortwave, longwave and net radiative divergence (middle) and convective velocity scale (bottom) for the entire day.

Figure 7: Averaged profile of vertical velocity variance (top left) and vertical velocity skewness (top right). The updraft and downdraft fractions are shown in the bottom panels with thresholds

of 0 m s^{-1} (black), 0.25 m s^{-1} (red), 0.50 m s^{-1} (green), 0.75 m s^{-1} (blue) and 1 m s^{-1} (magenta). The thresholds are similar in magnitude but negative for the downdraft fraction.

Figure 8: Averaged profile of coherent updrafts and downdraft velocity (left) and averaged profile of updraft mass-flux (right).

Figure 9: Averaged profile of velocity binned mass-flux at 1200 m (top), 900 m, 600 m and 300 m (bottom). The updraft mass-flux at each level is also reported in the respective panels.

Figure 10: Radiative flux and heating rate profiles during coupled conditions (top panels) and during decoupled conditions (bottom panels).

Figure 11: Averaged profile of vertical velocity variance (left) and skewness (right) during coupled and decoupled conditions.

Figure 12: Updraft fraction (left) and downdraft fraction (right) for coupled conditions (top) and decoupled conditions (bottom). The velocity thresholds are 0 ms^{-1} (black), 0.25 ms^{-1} (red), 0.50 (green), 0.75 ms^{-1} (blue) and 1 ms^{-1} (magenta).

Figure 13: Vertical profile of coherent updrafts and coherent downdrafts (left) and mass-flux (right) for coupled and decoupled conditions.

Figure 14: Velocity binned mass-flux at 1200 m (top), 900 m, 600 m and 300 m (bottom) for coupled and decoupled conditions. The updraft mass-flux for the distinction is also reported in each panel.

Figure 15: Profile of vertical velocity variance, updraft mass-flux, coherent updrafts and coherent downdrafts scaled by the convective velocity scale during coupled and decoupled conditions.

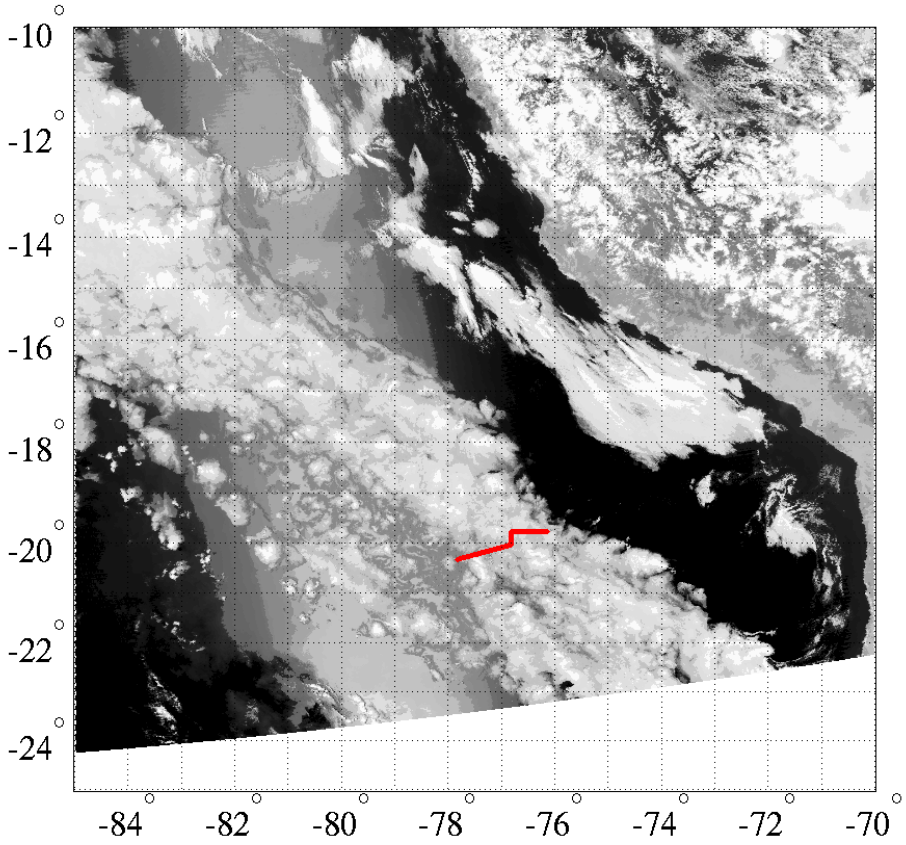

Figure 1: Visible image as captured by the MODIS Aqua satellite on 27 November 2008 at 1855 UTC (1255 local time). The red line shows the eastward track of the Ronald H. Brown for that day.

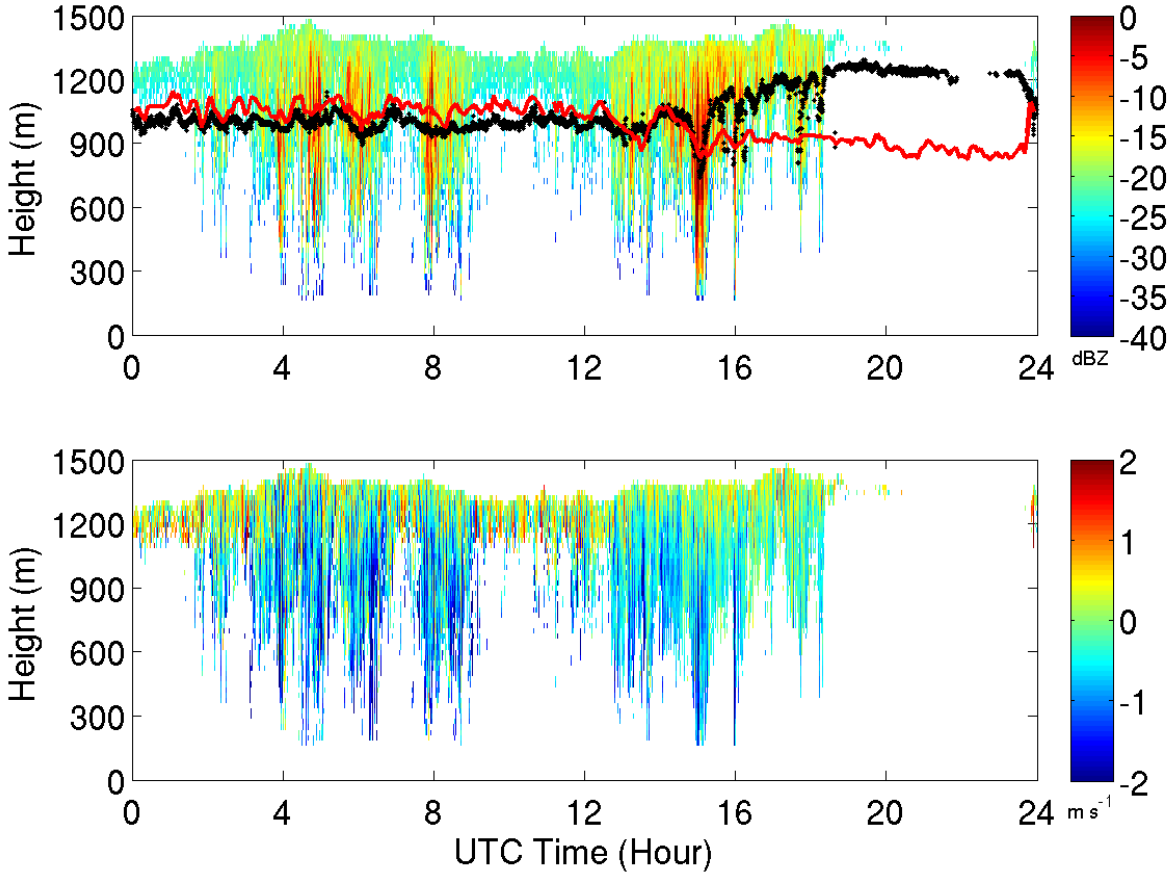

Figure 2: Reflectivity (top) and mean Doppler velocity (bottom) as recorded by the vertically pointing 95 GHz Doppler Cloud radar on 27 November 2008. The ceilometer recorded cloud base height is shown in black while the lifting condensation level calculated using surface measurements is shown in red.

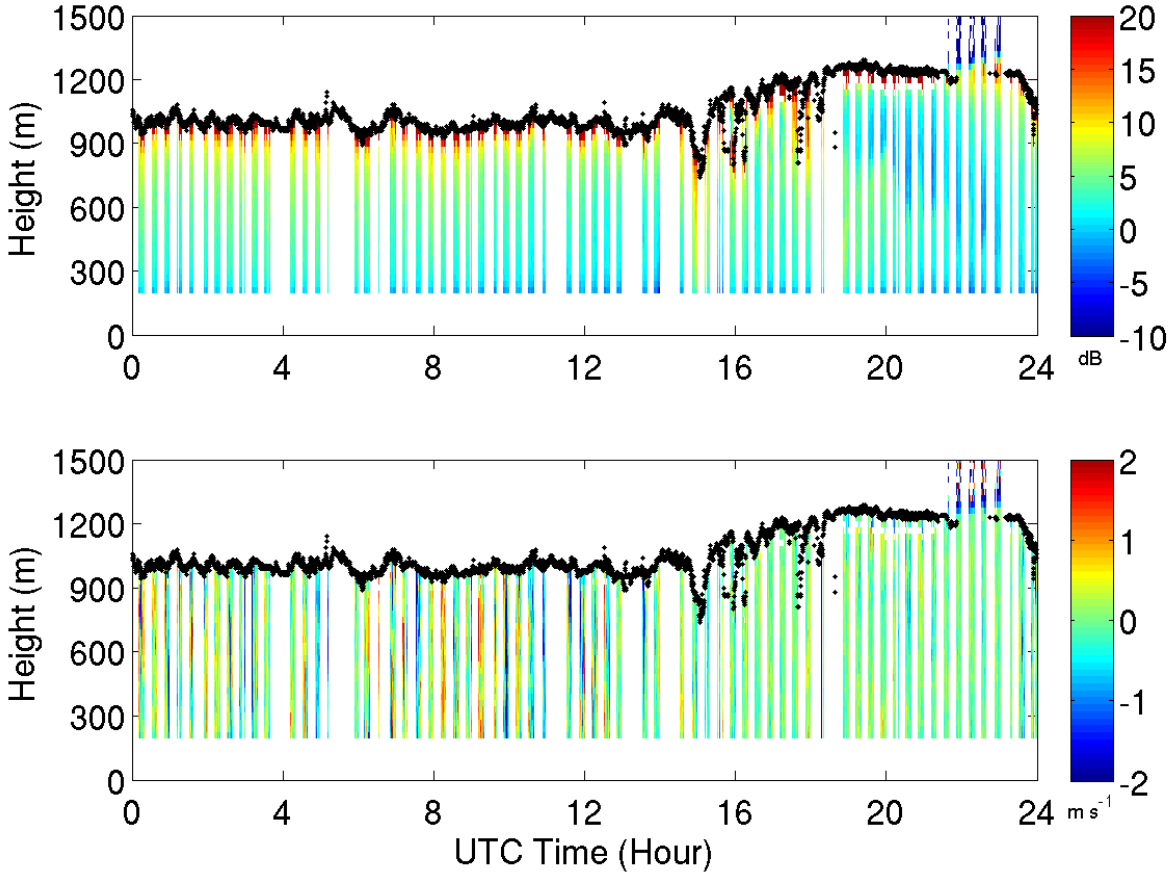

Figure 3: The signal to noise ratio (top) and Doppler velocity (bottom) as recorded by the HRDL when it was pointing vertically upwards on 27 November 2008. The ceilometer recorded cloud base height is shown in black.

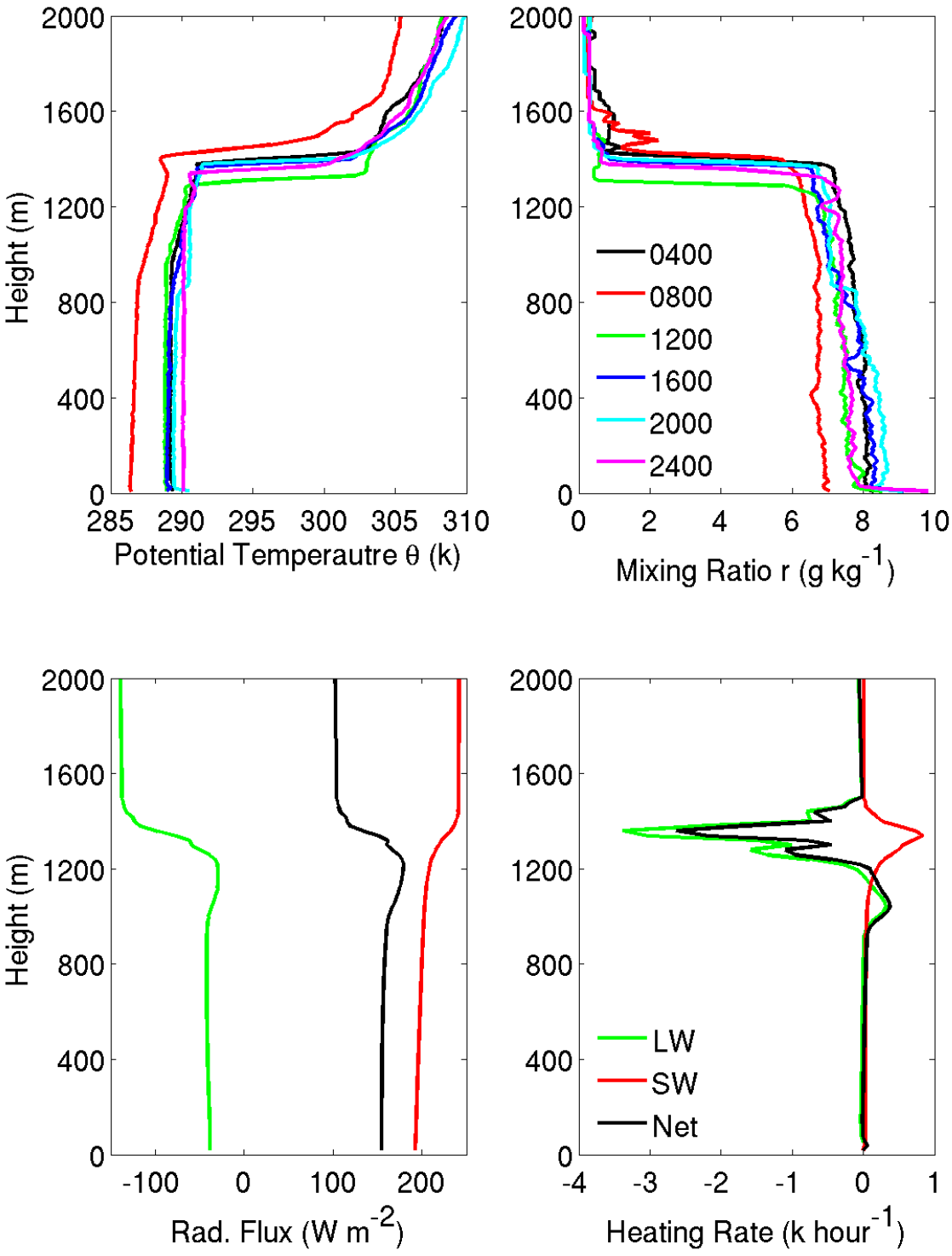
Height (m)
Potential Temperautre θ (k)
Mixing Ratio r (g kg-1)
0400
0800
1200
1600
2000
2400
Rad. Flux (W m-2)
Heating Rate (k hour-1)
LW
SW
Net

1

Figure 4: Profiles of potential temperature and mixing ratio (top panels) as reported by the radiosondes launched during that day and profiles of averaged longwave (LW), shortwave (SW) and net radiative flux along with the associated heating rates (bottom panels).

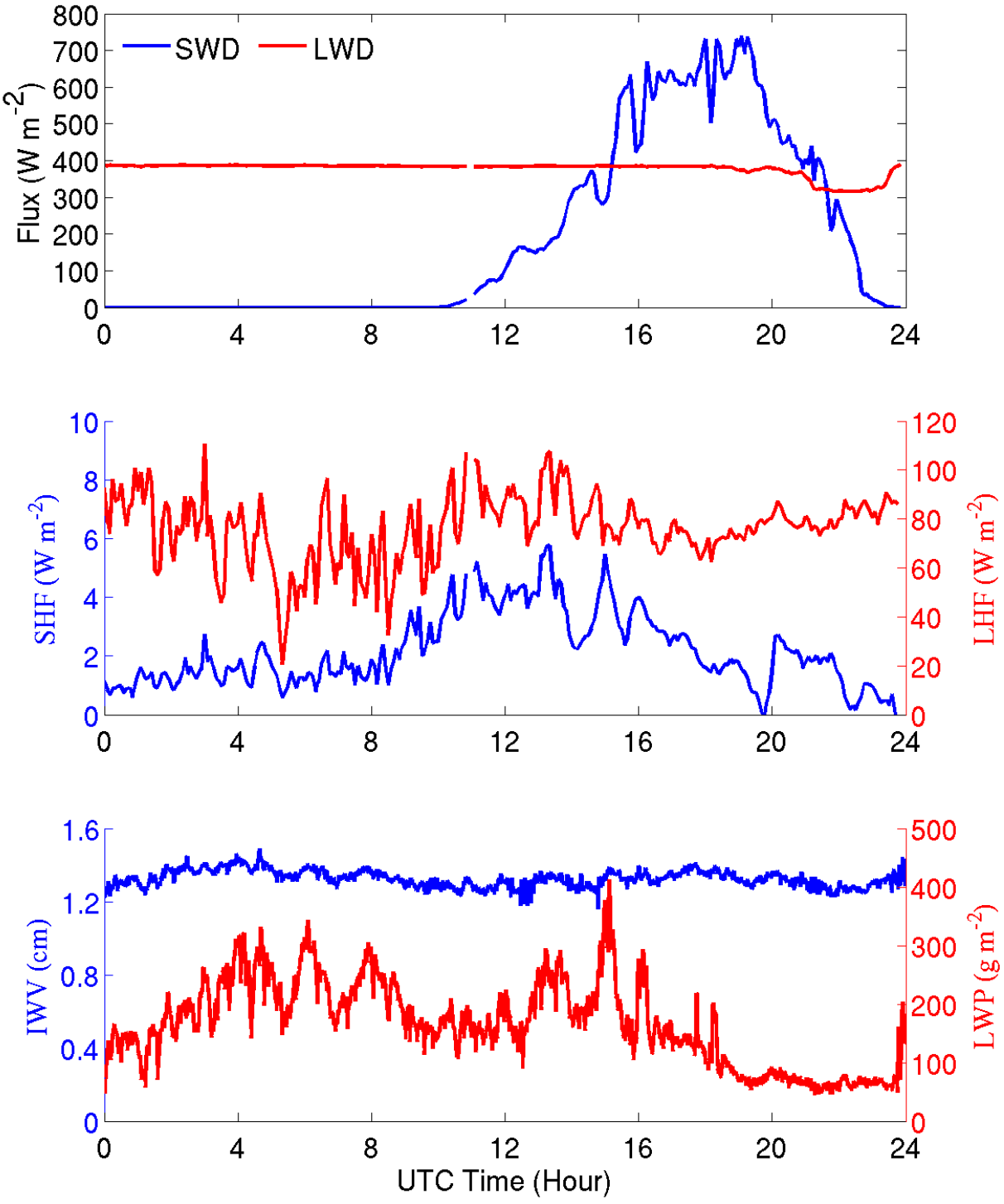

1

Figure 5: Downwelling shortwave radiation and downwelling longwave radiation (top), surface sensible heat flux and surface latent heat flux (middle) and integrated water vapor and liquid water path (bottom) for 27 November 2008. The local time is six hours behind UTC.

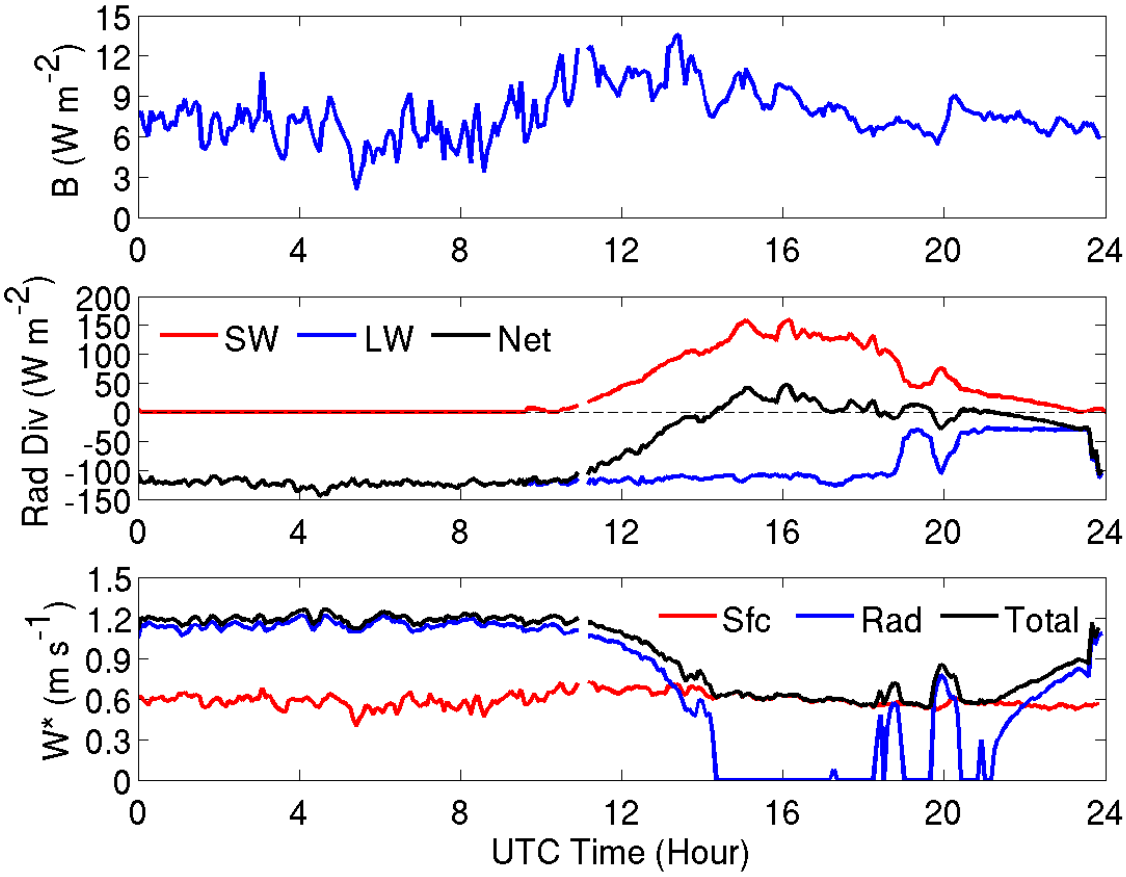

Figure 6: Surface buoyancy flux (top), shortwave, longwave and net radiative divergence (middle) and convective velocity scale (bottom) for the entire day.

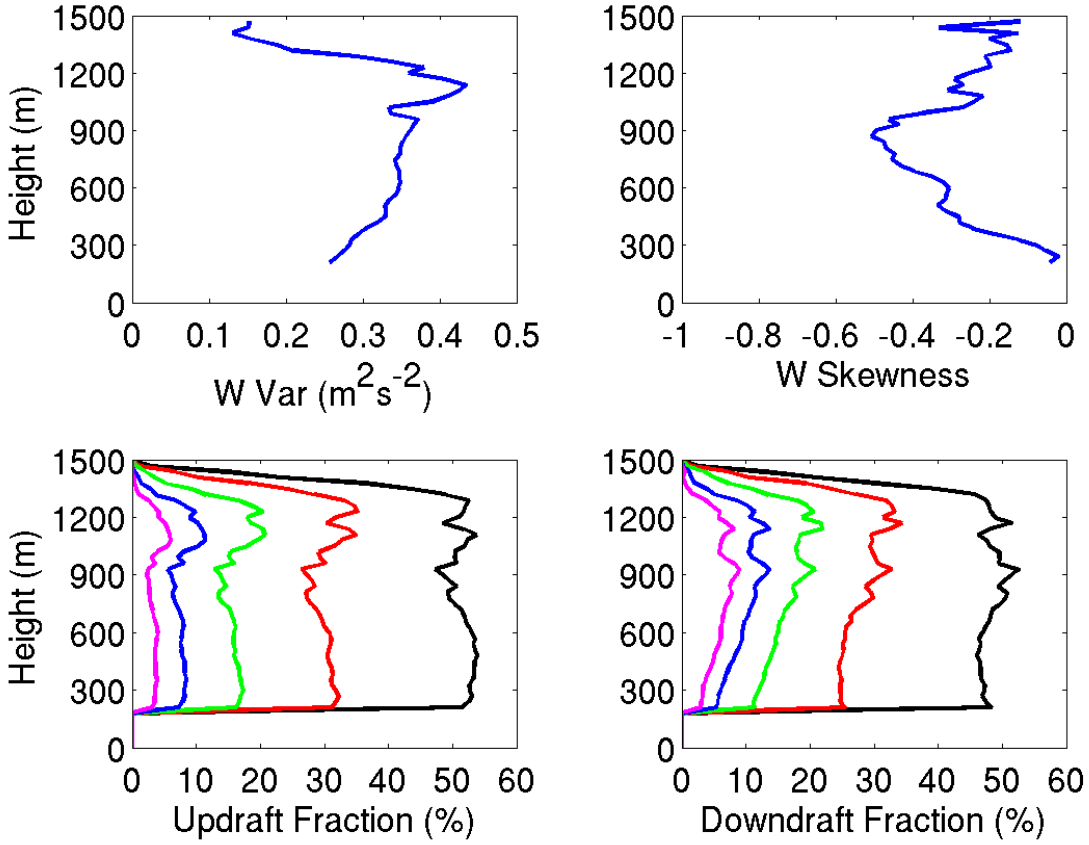

Figure 7: Averaged profile of vertical velocity variance (top left) and vertical velocity skewness (top right). The updraft and downdraft fractions are shown in the bottom panels with thresholds of 0 ms^{-1} (black), 0.25 ms^{-1} (red), 0.50 ms^{-1} (green), 0.75 ms^{-1} (blue) and 1 ms^{-1} (magenta). The thresholds are similar in magnitude but negative for the downdraft fraction.

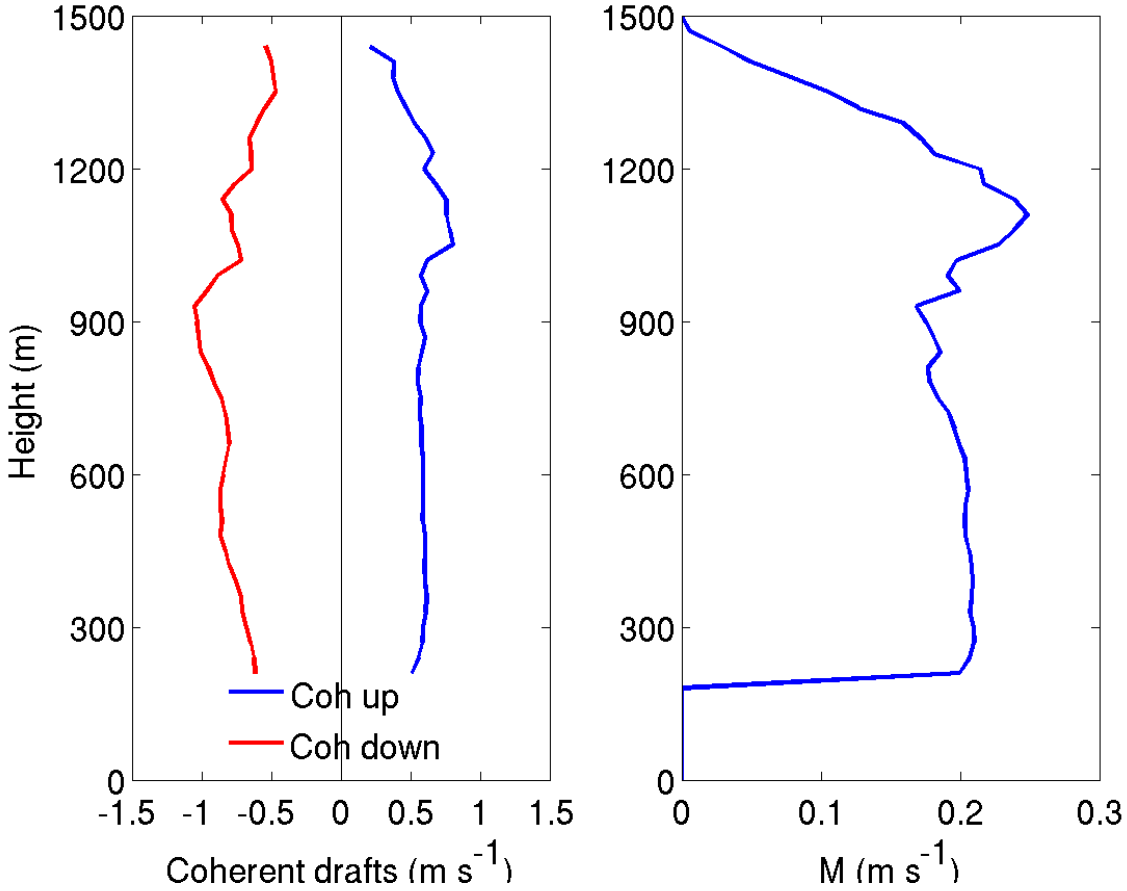

Figure 8: Averaged profile of coherent updrafts and downdraft velocity (left) and averaged profile of updraft mass-flux (right).

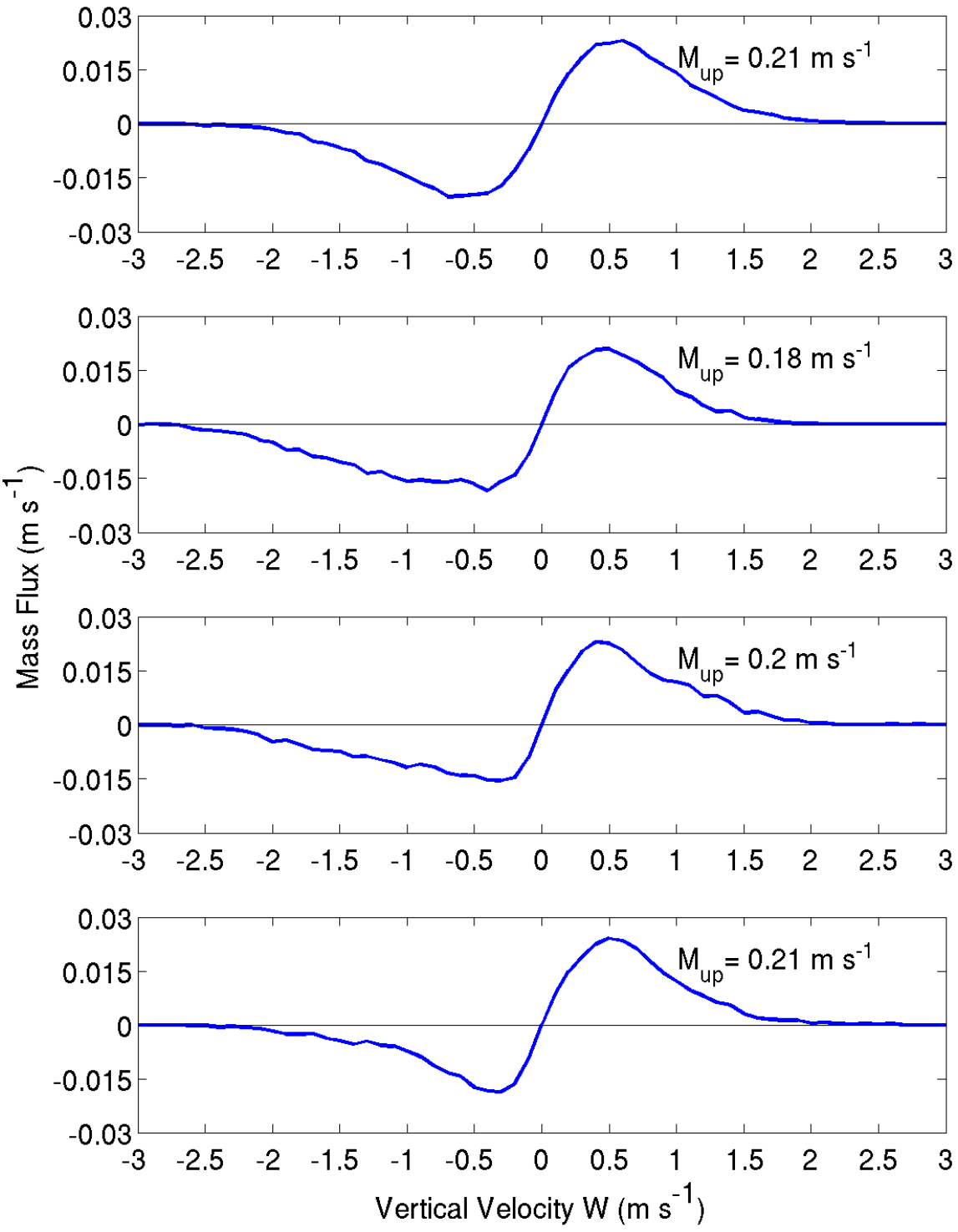
0.03
0.015
0
-0.015
-0.03
-3 -2.5 -2 -1.5 -1 -0.5 0 0.5 1 1.5 2 2.5 3
M_up= 0.21 m s-1
M_up= 0.18 m s-1
M_up= 0.2 m s-1
M_up= 0.21 m s-1
Mass Flux (m s-1)
Vertical Velocity W (m s-1)

1

Figure 9: Averaged profile of velocity binned mass-flux at 1200 m (top), 900 m, 600 m and 300 m (bottom). The updraft mass-flux at each level is also reported in the respective panels.

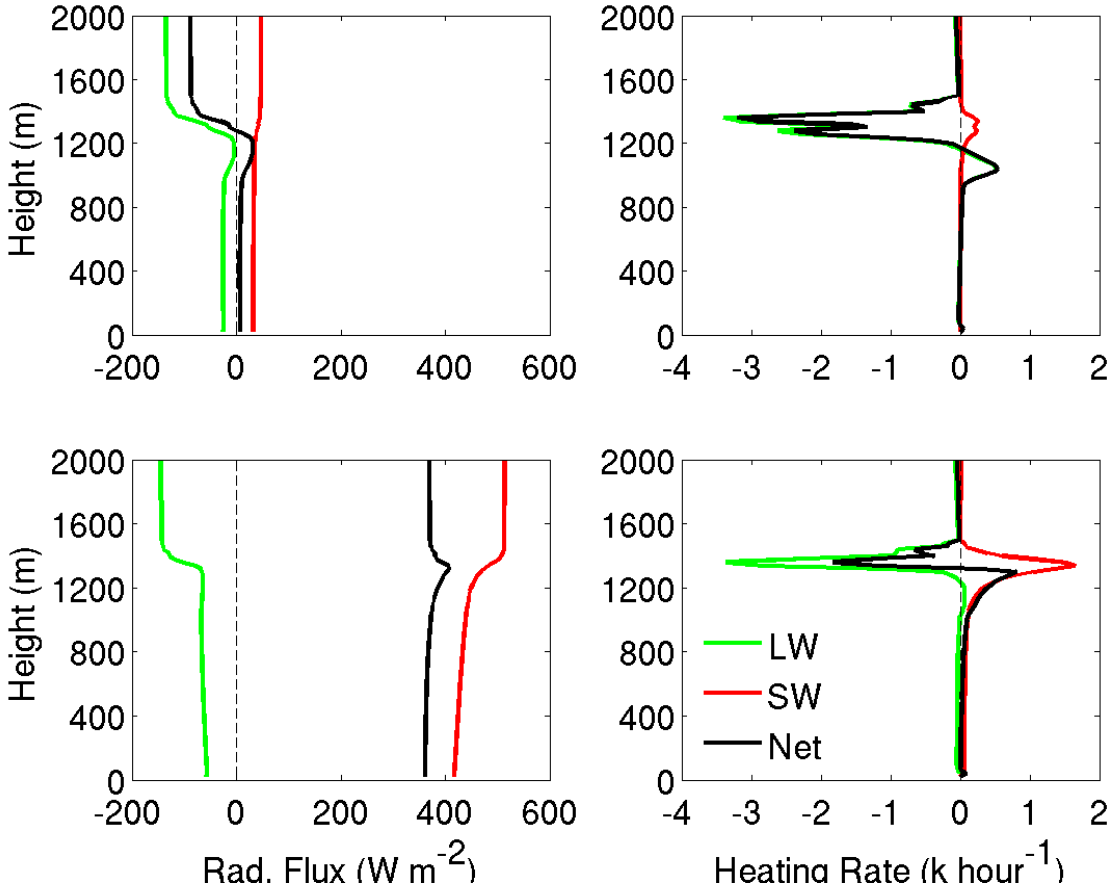

Figure 10: Radiative flux and heating rate profiles during coupled conditions (top panels) and during decoupled conditions (bottom panels).

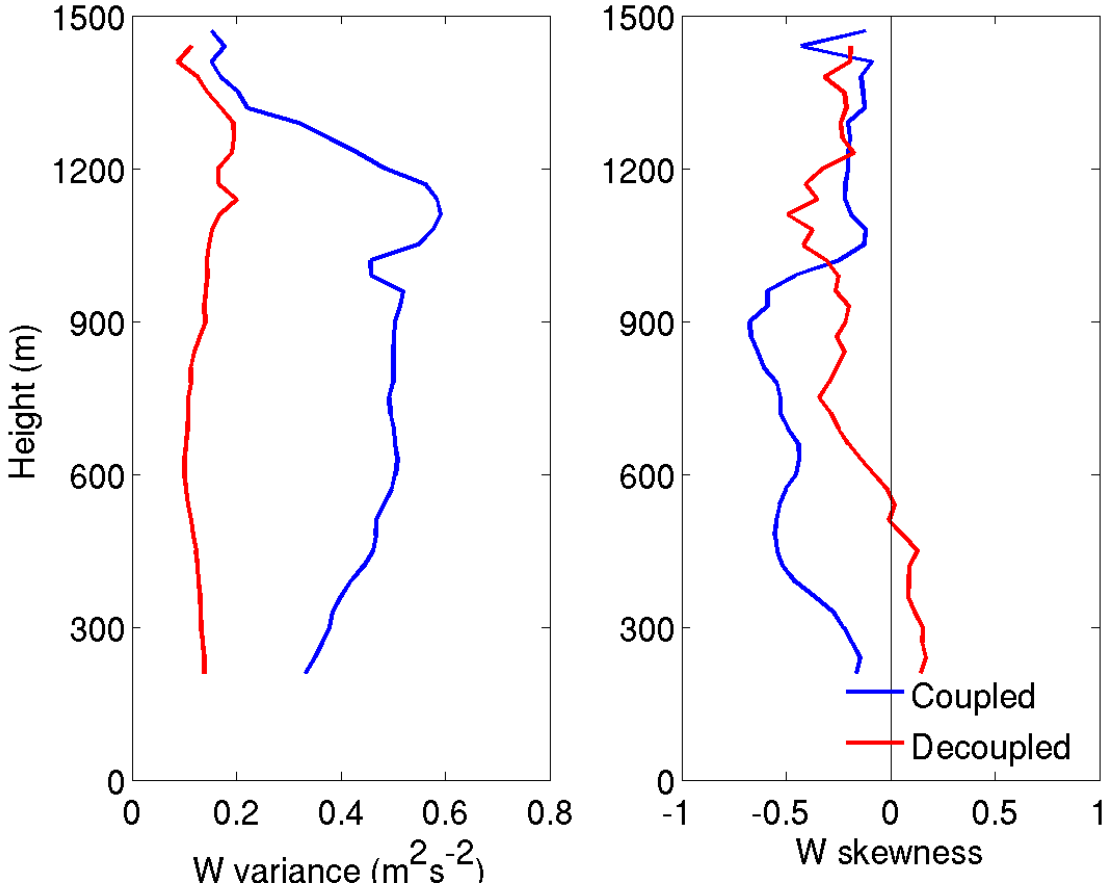

Figure 11: Averaged profile of vertical velocity variance (left) and skewness (right) during coupled and decoupled conditions.

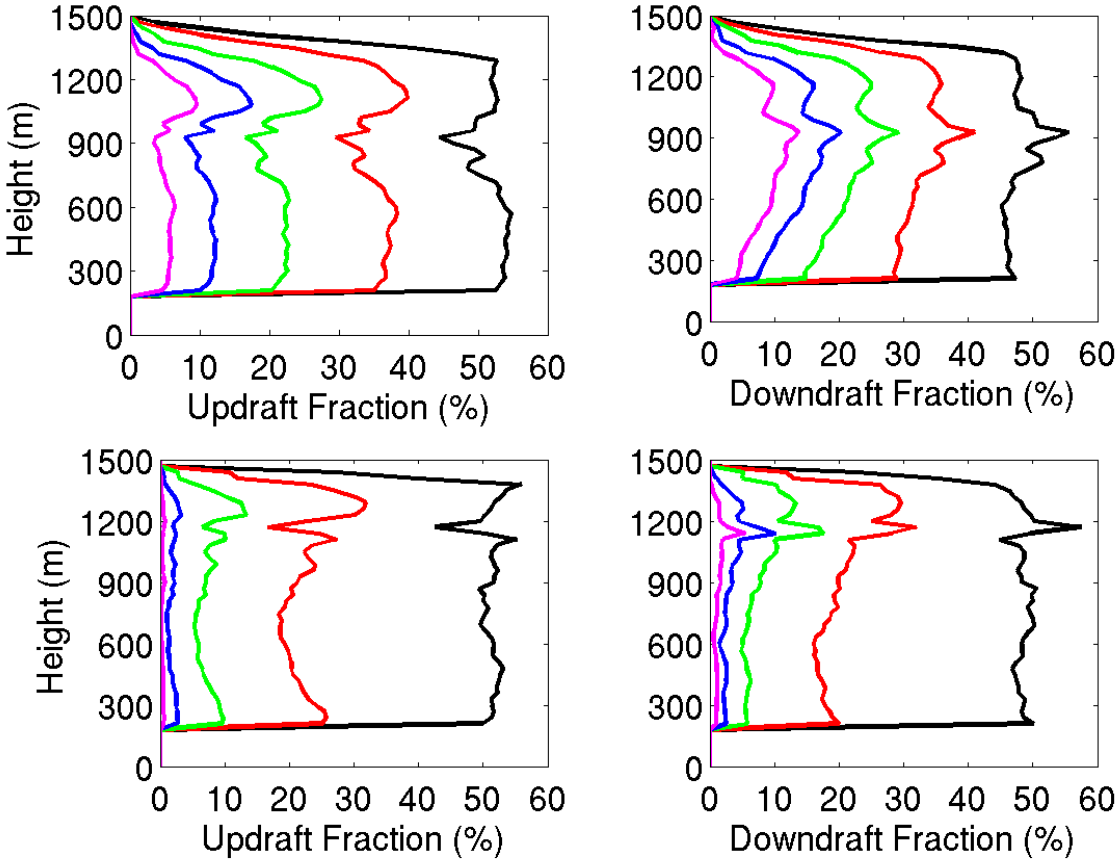

Figure 12: Updraft fraction (left) and downdraft fraction (right) for coupled conditions (top) and decoupled conditions (bottom). The velocity thresholds are 0 m s^{-1} (black), 0.25 m s^{-1} (red), 0.50 m s^{-1} (green), 0.75 m s^{-1} (blue) and 1 m s^{-1} (magenta).

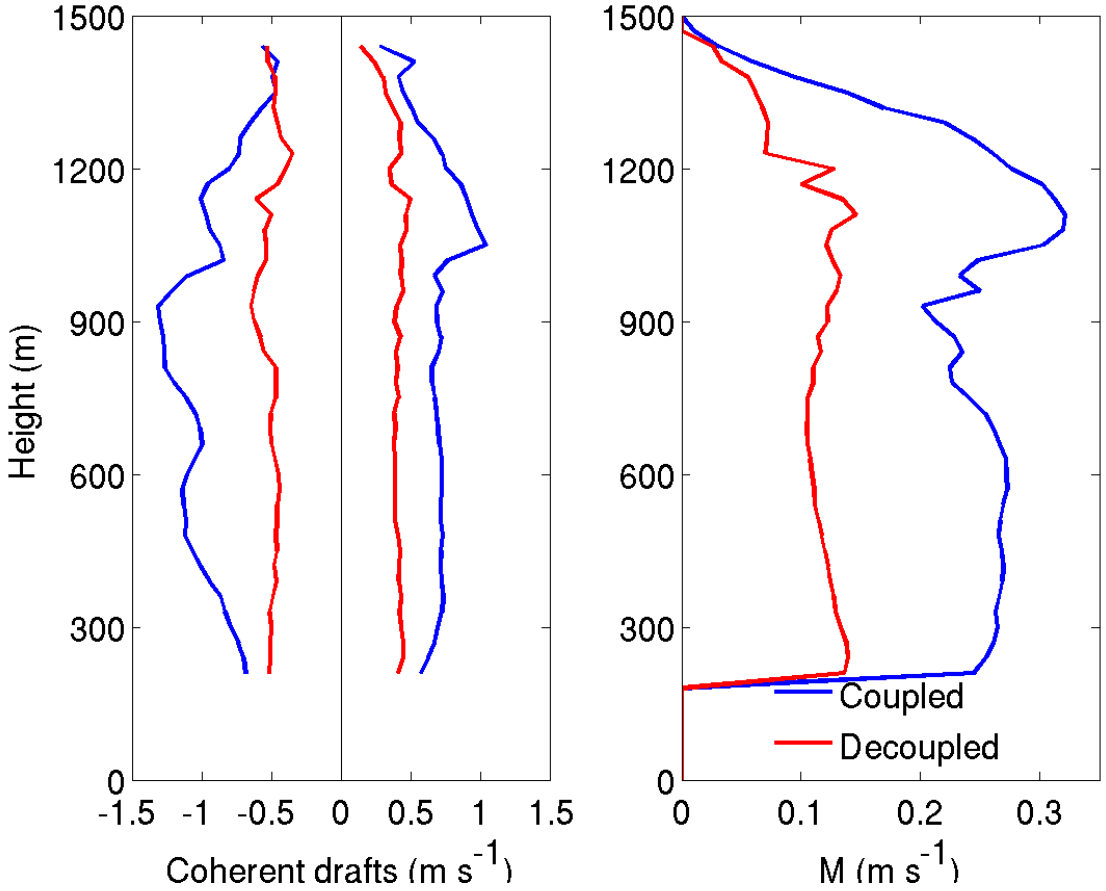

Figure 13: Vertical profile of coherent updrafts and coherent downdrafts (left) and mass-flux (right) for coupled and decoupled conditions.

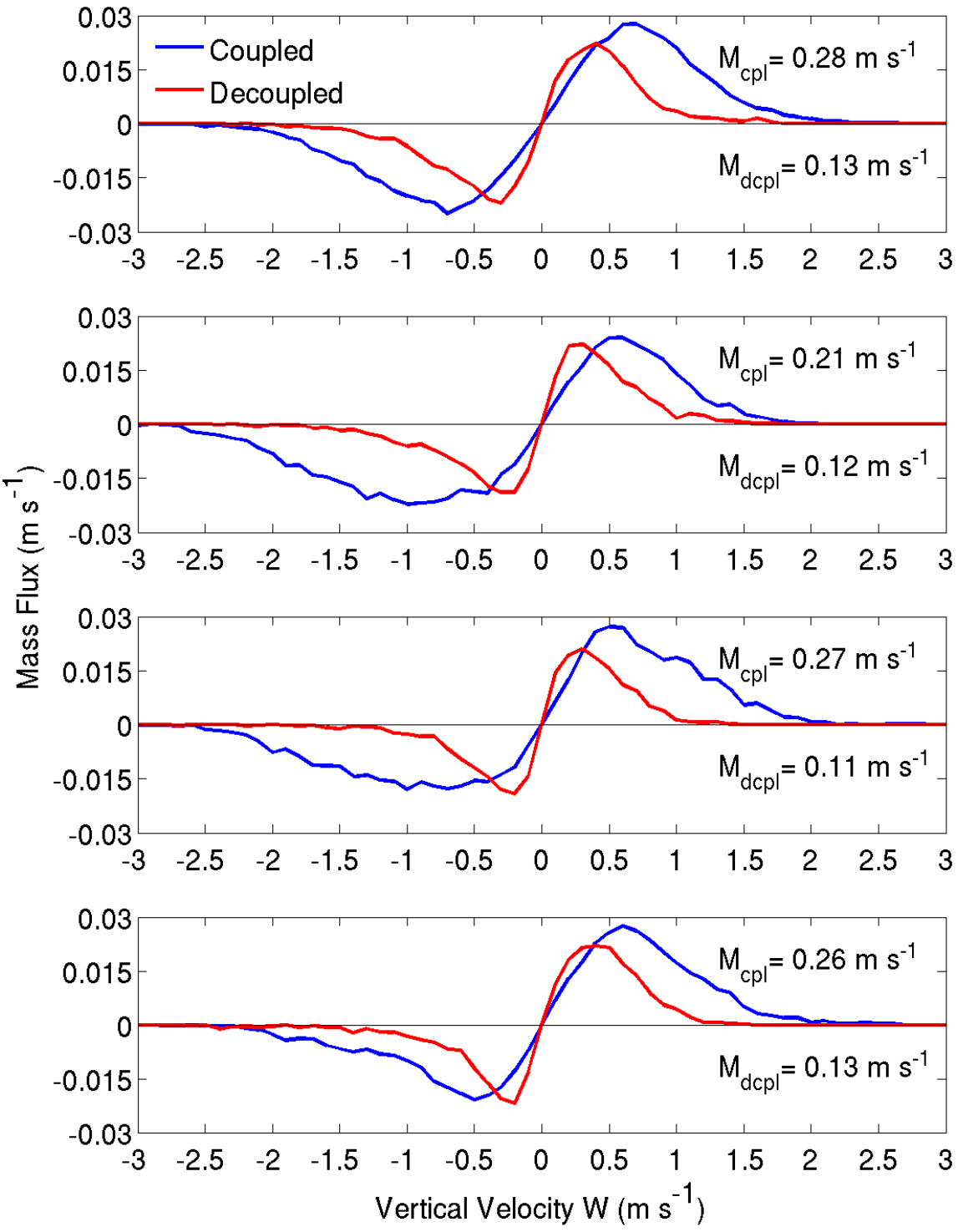
Coupled
Decoupled
M_{cpl}= 0.28 m s^{-1}
M_{dcpl}= 0.13 m s^{-1}
M_{cpl}= 0.21 m s^{-1}
M_{dcpl}= 0.12 m s^{-1}
M_{cpl}= 0.27 m s^{-1}
M_{dcpl}= 0.11 m s^{-1}
M_{cpl}= 0.26 m s^{-1}
M_{dcpl}= 0.13 m s^{-1}
Mass Flux (m s^{-1})
Vertical Velocity W (m s^{-1})
0.03
0.015
0
-0.015
-0.03
-3 -2.5 -2 -1.5 -1 -0.5 0 0.5 1 1.5 2 2.5 3

1

Figure 14: Velocity binned mass-flux at 1200 m (top), 900 m, 600 m and 300 m (bottom) for coupled and decoupled conditions. The updraft mass-flux for the distinction is also reported in each panel.

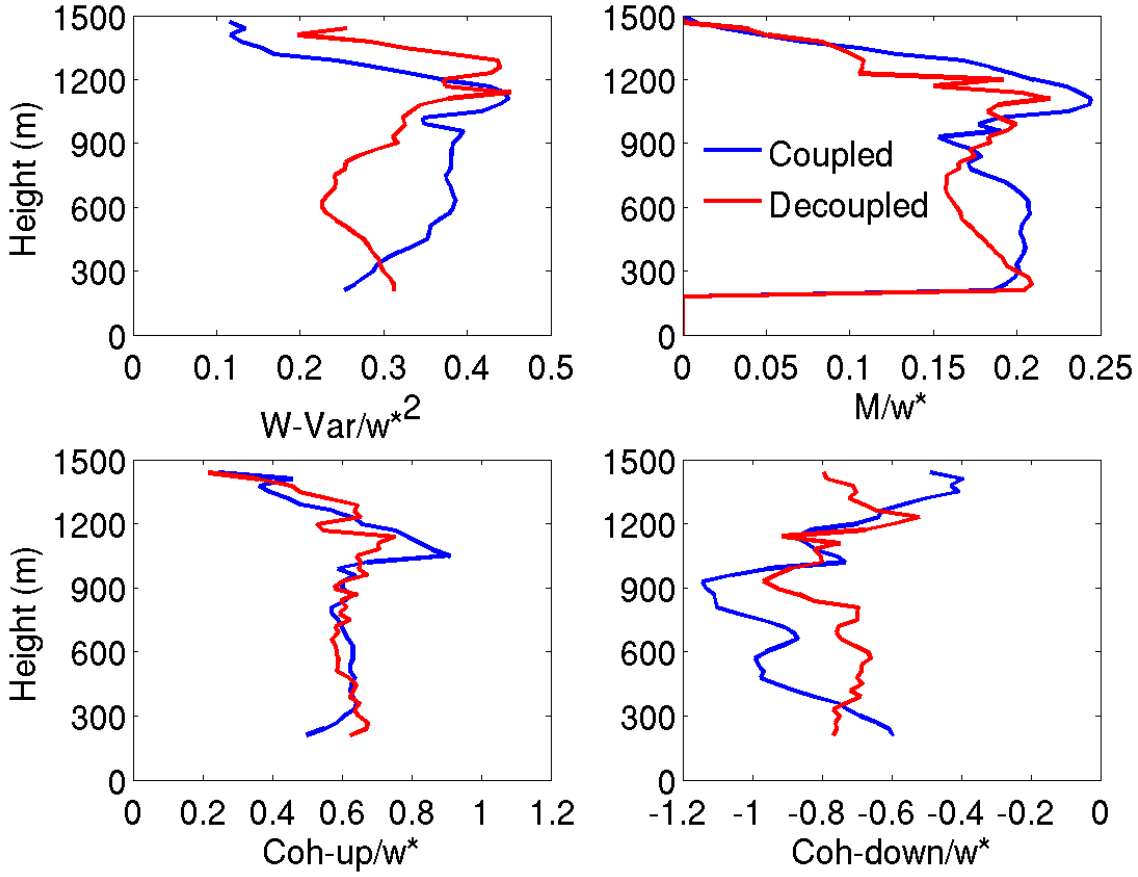

Figure 15: Profile of vertical velocity variance, updraft mass-flux, coherent updrafts and coherent downdrafts scaled by the convective velocity scale during coupled and decoupled conditions.